catalysts

MDPI

Review

A Review on Quantum Dots Modified g-C_3N_4-Based Photocatalysts with Improved Photocatalytic Activity

Yanling Chen and Xue Bai *

Key Laboratory of Integrated Regulation and Resource Development on Shallow Lake of Ministry of Education, College of Environment, Hohai University, Nanjing 210098, China; chenyanling@hhu.edu.cn

* Correspondence: baixue@hhu.edu.cn; Tel.: +86-159-5194-0543

Received: 13 December 2019; Accepted: 15 January 2020; Published: 20 January 2020

Abstract: In the 21st century, the development of sustainable energy and advanced technologies to cope with energy shortages and environmental pollution has become vital. Semiconductor photocatalysis is a promising technology that can directly convert solar energy to chemical energy and is extensively used for its environmentally-friendly properties. In the field of photocatalysis, graphitic carbon nitride (g-C_3N_4) has obtained increasing interest due to its unique physicochemical properties. Therefore, numerous researchers have attempted to integrate quantum dots (QDs) with g-C_3N_4 to optimize the photocatalytic activity. In this review, recent progress in combining g-C_3N_4 with QDs for synthesizing new photocatalysts was introduced. The methods of QDs/g-C_3N_4-based photocatalysts synthesis are summarized. Recent studies assessing the application of photocatalytic performance and mechanism of modification of g-C_3N_4 with carbon quantum dots (CQDs), graphene quantum dots (GQDs), and g-C_3N_4 QDs are herein discussed. Lastly, challenges and future perspectives of QDs modified g-C_3N_4-based photocatalysts in photocatalytic applications are discussed. We hope that this review will provide a valuable overview and insight for the promotion of applications of QDs modified g-C_3N_4 based-photocatalysts.

Keywords: graphitic carbon nitride (g-C_3N_4); quantum dots (QDs); photocatalysis; H_2 production; organic pollutant photodegradation; CO_2 reduction

1. Introduction

With rapid urban and societal development, environmental pollution and energy demands have become two major global challenges, attracting increasing research attention [1–3]. Sunlight-driven photocatalytic technologies provide a promising method to solve these problems [4–6]. As a novel strategy to take advantage of solar energy, semiconductor photocatalysts are becoming a scientific research focus due to its environmentally-friendly and energy-efficient characteristics, as compared to biological and chemical methods [7–10]. In recent years, various semiconductor photocatalysts, including TiO_2 [11], boron nitride [12], black phosphorus [13], ZnO [14], and Bi_2WO_6 [15] have been synthetized and widely studied with the application in H_2 production [16–21], organic pollutants photodegradation [22–26], CO_2 reduction [27,28], and other fields.

As a metal-free semiconductor with a typical two-dimensional structure, graphitic carbon nitride (g-C_3N_4) has received high levels of attention since Wang et al. [29] first reported that g-C_3N_4 exhibited excellent photocatalytic performance in water splitting under visible light irradiation in 2009. These findings contributed to the evidence that g-C_3N_4 not only has relatively high thermal and chemical stability due to its tri-s-triazine ring structure and high degree of polymerization [30–32], but also possesses an appropriate band gap (2.7 eV) and conduction band (CB) position (1.07 eV) [33,34]. However, a high recombination rate of photogenerated charge carriers occurs because of the weak van der Waals interactions between neighboring CN layers [35], a small specific area [36–39], narrow

visible-light absorption [40], and low quantum efficiency [25]. This greatly limits the photocatalytic activity of pure g-C_3N_4, which hinders its practical applications. To improve the photocatalytic activity of g-C_3N_4, various strategies have been developed, including nonmetal doping [41–43], passivation layer deposition [44–46], metal deposition [47], morphology control [48–53], constructing heterojunction structures [54–60], and modification by carbonaceous nanomaterials such as rGO, GO, carbon nanospheres, and carbon dots [61–64].

Because of their unique size, dependent properties, and well-defined electronic and optical properties, quantum dots (QDs) have become a key research focus [65–67]. Carbon quantum dots (CQDs) are an emerging zero-dimensional (0D) carbon-based nanomaterial with an average size below 10 nm. CQDs have attracted more research attention than traditional semiconductor QDs due to their unique and beneficial optical and electronic properties [68–71], such as aqueous solubility, up-conversion photoluminescence (PL) characteristics, photo-induced electron transfer properties, size effect, conductivity, photochemical stability, low cost, and non-toxicity [72–76]. Therefore, CQDs have been applied as an efficient component in the design of photocatalysts. Based on successful coupling with semiconductor photocatalysts (such as TiO_2 and ZnO), the catalytic activity of CQDs have been improved by inhibiting photogenerated carrier recombination [77–80]. CQDs also can broaden the visible light absorption range for other semiconductor photocatalysts (such as Si, Ag_3PO_4, CdS, and Bi_2WO_6) [81–84]. In addition, the conjugated π structure of CQDs can enhance their interaction with semiconductors to form stable composites [85]. Therefore, CQDs have been widely used in various fields of study, such as photocatalysis [86], biosensing [87], and chemiluminescence analysis [88].

Considering the unique properties of g-C_3N_4 and CQDs, an increasing body of research has attempted to couple g-C_3N_4 with CQDs to fabricate new photocatalysts to improve their photocatalytic performance. In recent years, CQDs modified g-C_3N_4 has been widely applied in H_2 evolution [89,90], the degradation of organic pollutants [91–96], CO_2 reduction [97], and disinfection [98], which exhibits excellent photocatalytic performance. As depicted in Figure 1, besides CQDs, graphene quantum dots (GQDs) and g-C_3N_4 QDs have also been used to modify g-C_3N_4. As shown in Figure 2, the number of papers related to QDs modified g-C_3N_4 photocatalysts has increased annually from 2010 to 2019, according to the statistics provided by Web of Science based on "g-C_3N_4," "graphitic carbon nitride," "quantum dots," "CQDs," and "GQDs" as keywords. However, a comprehensive summary of QDs modified g-C_3N_4-based photocatalysts remains absent.

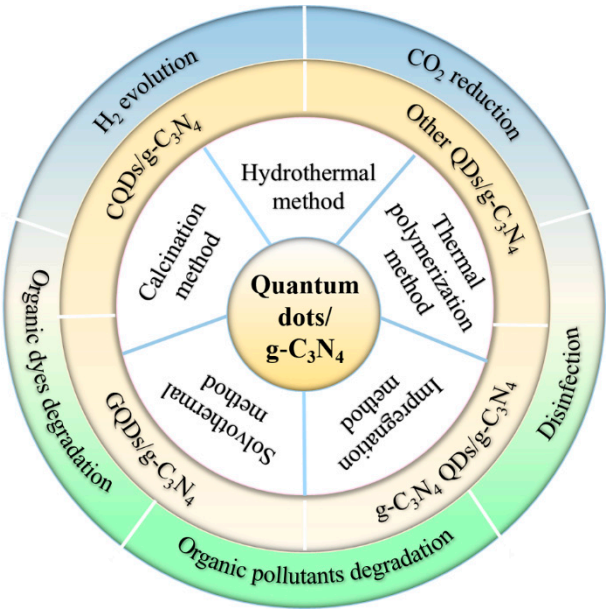

Figure 1. Summary diagram of the synthetic methods, classification, and applications of quantum dots/g-C_3N_4 photocatalysts.

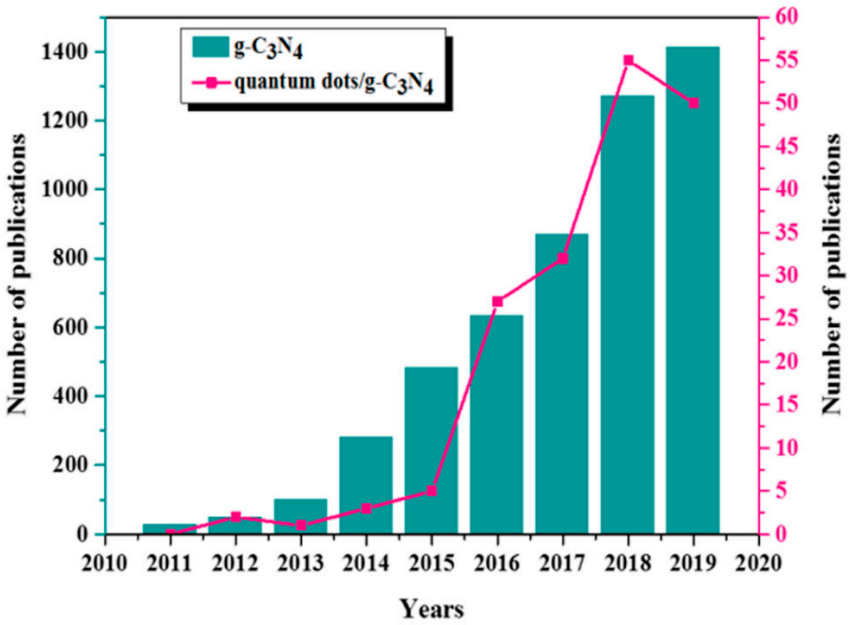

Figure 2. Number of publications of g-C_3N_4-related papers in terms of the keywords: "g-C_3N_4," "graphitic carbon nitride," and quantum dots/g-C_3N_4-related papers in terms of the keywords: "g-C_3N_4," "graphitic carbon nitride," "quantum dots," "CQDs," and "GQDs". Data refers to indexed journal publications between 2011 and 2019, as reported on "Web of Science."

The main purpose of this review was to summarize the recent progress in the combination of g-C_3N_4 with CQDs and other QDs, for the synthesis of new photocatalysts. We first summarize the latest fabrication strategies of QDs/g-C_3N_4-based photocatalysts and then elaborate on their application, photocatalytic performance, and the mechanism of formation of CQDs, GQDs, and g-C_3N_4 QDs modified g-C_3N_4 hybrids. Subsequently, other types of QDs modified g-C_3N_4-based photocatalysts are also presented. Lastly, the challenges, aspects requiring research focus, and the potential future development of QDs/g-C_3N_4-based photocatalysts in photocatalytic applications are discussed. This review enriches knowledge in the preparation methods, design, and application of QDs/g-C_3N_4-based photocatalysts and supports future research on the combination of g-C_3N_4 with other QDs for improved photocatalytic ability.

2. QDs/g-C_3N_4-Based Photocatalyst Synthesis Methods

Currently, various approaches have been developed to synthesize QDs/g-C_3N_4-based photocatalysts. A large body of research suggests that QDs modified g-C_3N_4 displays better photoactivity than pure g-C_3N_4. However, the synthesis methods have a great influence on the physical and chemical properties as well as on the photocatalytic performance of the produced photocatalysts. Table 1 shows various synthesis methods, applications, and the resulting photocatalytic efficiencies for QDs/g-C_3N_4-based photocatalysts.

Table 1. Synthetic methods, applications, and photocatalytic efficiency of QDs/g-C_3N_4 based photocatalysts.

Composites	Synthetic Methods	Applications	Light Source	Efficiency	Reference
CND/pCN	Hydrothermal	CO_2 reduction	500 W Xe lamp (>400 nm)	CO evolution rate: 5.9 μmol g^{-1} h^{-1} CH_4 evolution rate: 2.9 μmol g^{-1} h^{-1}	[75]
NCD/g-C_3N_4	Hydrothermal-polymerized	Degradation of IDM	Visible light	91.5% IDM in 90 min	[90]
BiOBr/CDs/g-C_3N_4	Hydrothermal	Degradation of CIP	300 W Xe lamp	82.7% CIP in 60 min	[91]
CDs/g-C_3N_4	Hydrothermal	H_2 evolution	3 W LEDs at 365 nm	2.2 μmol h^{-1}	[92]
Pt-CDs/g-C_3N_4	Photoreduction	H_2 evolution	Visible light at 420 nm	183.0 μmol h^{-1}	[92]
CQDs/g-C_3N_4	Facile low temperature process	Degradation of Rh B and TC-HCl	250 W Xe lamp at 420 nm	95.2% Rh B and 78.6% TC-HCl in 3.5 h	[95]
CDs/g-C_3N_4	Impregnation-thermal	Degradation of phenol	300W Xe lamp (<400 nm)	100% phenol in 200 min	[96]
Nonpolar CQDs/g-C_3N_4	Water vapor at room temperature	CO_2 reduction	300 W Xe lamp at 400 nm	CO evolution rate: 23.4 μmol g^{-1} h^{-1} CH_4 evolution rate: 20.8 μmol g^{-1} h^{-1}	[97]
CQDs/g-C_3N_4	Impregnation	Inactivation of *Staphylococcus aureus*	Visible light	-	[98]
g-C_3N_4 NSs/CQDs	Hydrothermal	H_2 evolution	300 W Xe lamp at 420 nm	88.1 μmol h^{-1}	[99]
CDs/g-C_3N_4/MoO_3	Calcination	Degradation of TC	350 W Xe lamp at 420 nm	88.4% TC in 90 min	[100]
CQD-implanted g-C_3N_4 NTs	Thermal polymerization	H_2 evolution	Visible light	3538.3 mmol g^{-1} h^{-1}	[101]
CDs/g-C_3N_4	In situ thermal polymerization	H_2 evolution	300 W Xe lamp (>420 nm)	2.34 mmol g^{-1} h^{-1}	[102]
g-C_3N_4 NSs/CQDs	Solvothermal	H_2 evolution	500 W Xe lamp (>420 nm)	116.1 μmol h^{-1}	[103]
S-CQDs/HTCN-C	Ultrasonic assisted method	Inactivation of *Escherichia coli*	300W Xe lamp	99.99% *Escherichia coli* in 40 min	[104]
CDs/CdS QDs/g-C_3N_4	Solvothermal-coprecipitation	H_2 evolution	300 W Xe lamp (>420 nm)	9.4 μmol g^{-1} h^{-1}	[105]

Table 1. *Cont.*

Composites	Synthetic Methods	Applications	Light Source	Efficiency	Reference
CQDs/g-C_3N_4	electrostatic self-assembly strategy	Degradation of MB	Visible light	-	[106]
CDs/g-C_3N_4/ZnO	Impregnation-thermal	Degradation of TC	Xe lamp (<420 nm)	100% TC in 30 min	[107]
CDs/g-C_3N_4/TiO_2	Impregnation precipitation	H_2 evolution	350W Xe lamp	-	[108]
Fe(III)/CQDs/Fe-CN	Impregnation	Degradation of MO	300 W Xe lamp at 420 nm	93% MO in 60 min	[109]
GA-CQDs/CNN	Two-step hydrothermal	Degradation of MO	Visible light	91.1% MO in 4 h	[110]
g-C_3N_4/ZnTcPc/GQDs	Hydrothermal	Degradation of Rh B	Solar light	98.2% Rh B in 60 min	[111]
GQDs/g-CNNR	Hydrothermal	Removal of antibiotics	300 W Xe lamp	80% antibiotics in 120 min	[112]
g-C_3N_4/BCNQDs	Molten salt	H_2 evolution	300 W Xe lamp	70.05 mmol h^{-1}	[113]
Sb_2S_3/g-C_3N_4/CNS	Hydrothermal	Degradation of MO	300 W Xe lamp	0.0103 MO min^{-1}	[114]
MoS_2/CdS QDs/g-C_3N_4 NSs	Hydrothermal and chemical bath deposition-calcination	H_2 evolution, Degradation of Rh B and BPA	Visible light	956 μmol h^{-1} g^{-1}, 99% Rh B and 95.2% BPA in 20 min	[115]
Bi_2WO_6 QDs/g-C_3N_4	One-pot hydrothermal	Degradation of Rh B	Xe lamp	almost 100% Rh B in 30 min	[116]
Ag QDs/g-C_3N_4	One-step	H_2 evolution	300 W Xe lamp (>420 nm)	18.09 μmol g^{-1} h^{-1}	[117]
BP@g-C_3N_4	Electrostatic attraction	CO_2 reduction	300 W Xe lamp	6.54 μmol g^{-1} h^{-1}	[118]
Vanadate QDs/g-C_3N_4 NSs	In situ growth	Degradation of organic-dye	Visible light (>420 nm)	54% MO in 60 min	[119]
Fe_2O_3 QDs/g-C_3N_4	Calcination	Degradation of MB, MO, and Rh B	300 W Xe lamp	75% MB in 180 min	[120]
Co_3O_4 QDs/g-C_3N_4 NSs	Facile annealing process	Oxygen evolution reactions	300 W Xe lamp	20 μmol g^{-1} h^{-1}	[121]

Abbreviations: Carbon nanodot/g-C_3N_4 (CND/pCN). N-doped carbon dots/g-C_3N_4 (NCD/g-C_3N_4). Carbon quantum dots (CQDs). g-C_3N_4 nanosheets (g-C_3N_4 NSs). Carbon dots (CDs). g-C_3N_4 nanotubes (g-C_3N_4 NTs). Sulfur doped CQDs/hollow tubular g-C_3N_4 (S-CQDs/HTCN-C). Fe(III)/CQDs/Fe-doped g-C_3N_4 (Fe(III)/CQDs/Fe-CN). Graphene-CQDs/g-C_3N_4 nanosheet (GA-CQDs/CNN). Graphitic carbon nitride/zinc tetracarboxyphthalocyanine/graphene quantum dots (g-C_3N_4/ZnTcPc/GQDs). Graphene quantum dots modified graphitic carbon nitride nanorods (GQDs/g-CNNR). g-C_3N_4/B doped g-C_3N_4 QDs (g-C_3N_4/BCNQDs). Sb_2S_3/ultrathin g-C_3N_4 sheets/g-C_3N_4 QDs (Sb_2S_3/g-C_3N_4/CNS). Indomethacin (IDM). Ciprofloxacin (CIP). Tetracycline (TC). Methyl Orange (MO). Rhodamine B (Rh B). Bisphenol A (BPA).

2.1. Hydrothermal Method

The hydrothermal method is one of the most commonly used methods for synthesizing QDs/g-C_3N_4-based photocatalysts due to the low reaction temperature requirements. Ong et al. [75] used urea and glucose as precursors to synthesize metal-free 0D/2D carbon nanodot/g-C_3N_4 (CND/pCN) hybrid nanocomposites by a hydrothermal treatment at 120 °C. The CND/pCN-3 sample (3 wt.% of CND) showed the highest total evolutions of CH_4 (29.23 μmol $g_{catalyst}^{-1}$) and CO (58.82 μmol $g_{catalyst}^{-1}$) under visible light irradiation after 10 h of the reaction, which were 3.6 and 2.28 times higher than those generated with pCN, respectively. Overall, CND/pCN-3 demonstrated high stability and durability after four consecutive photoreaction cycles. Wang et al. [92] synthesized CDs/g-C_3N_4 via a facile hydrothermal approach (Figure 3). The generated CDs/g-C_3N_4 photocatalysts containing different amounts of carbon dots showed a red-shift in the absorption edge and an additional shoulder peak from 450 nm to 600 nm, compared with g-C_3N_4 (ca. 420 nm) (Figure 4a). The photocurrent of CDs/g-C_3N_4 (10 wt.%) was higher than that observed for g-C_3N_4, as shown in Figure 5a, which indicates that CDs can efficiently facilitate the interfacial charge transfer. The photocatalytic performance of CDs/g-C_3N_4 was evaluated and results suggested that 10 wt.% CDs/g-C_3N_4 showed the highest H_2 production rate (ca. 2.2 μmol h^{-1}), which was 4.4-fold more than that of g-C_3N_4 (ca. 0.5 μmol h^{-1}) under UV light irradiation. Liu et al. [99] prepared the 2D/0D ultrathin g-C_3N_4 nanosheets (UCN)/CQDs photocatalysts via a hydrothermal method using rapeseed flower bee pollens, dicyandiamide, and ammonium chloride as precursors. Results showed that coupling with CQDs extended the optical absorption of UCN to the near-infrared (NIR) region, which efficiently inhibited carrier recombination and enhanced the possibility of charge carriers participating in photocatalytic water splitting. The UCN/CQDs-0.2% composite exhibited optimal H_2 evolution of 88.1 μmol h^{-1}, 3.02-fold, and 1.91-fold greater than that of pristine UCN and bulk g-C_3N_4 (BCN)/CQDs-0.2%, respectively.

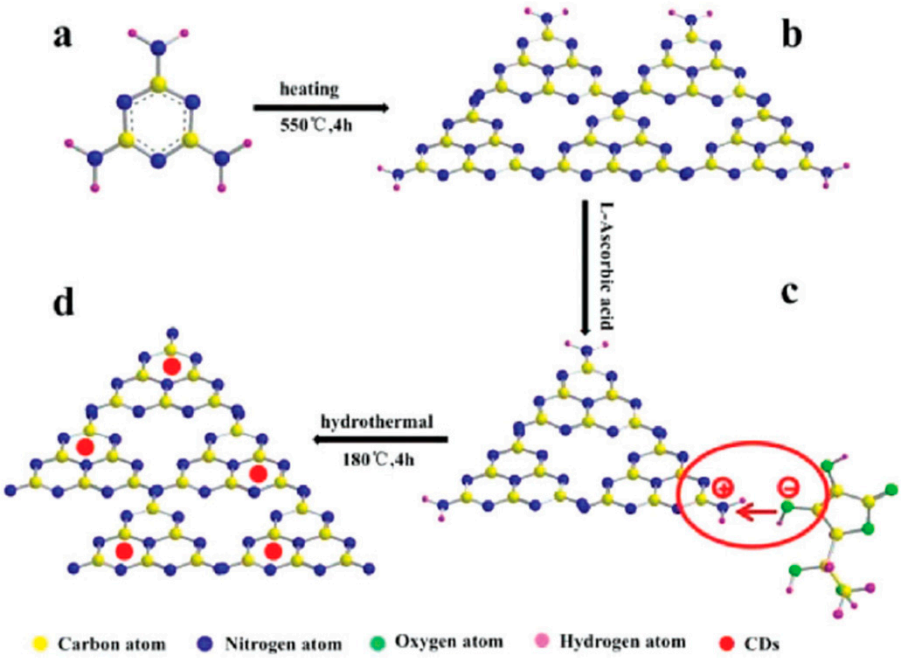

Figure 3. A schematic of the synthesis of CDs/g-C_3N_4: (**a**) melamine, (**b**) bulk g-C_3N_4, (**c**) L-ascorbic acid/bulk g-C_3N_4 complexes and (**d**) CDs/g-C_3N_4 (reproduced with permission from [92]. Copyright Royal Society of Chemistry, 2017).

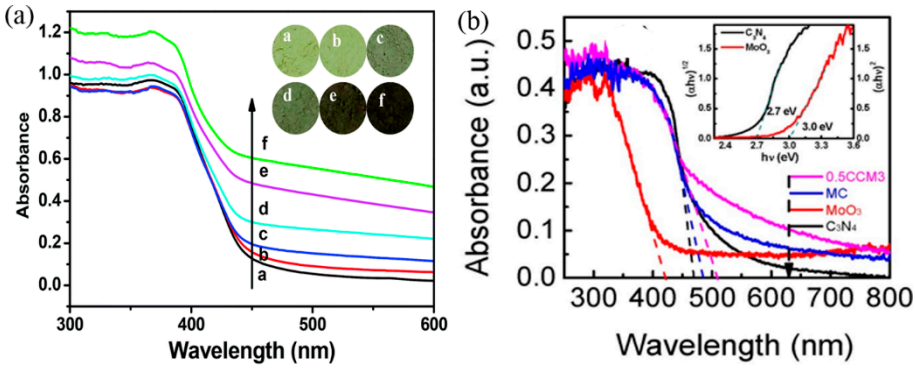

Figure 4. UV-vis diffuse reflectance absorbance spectra of (**a**) a–f: g-C_3N_4, CDs/g-C_3N_4 (1 wt.%), CDs/g-C_3N_4 (5 wt.%), CDs/g-C_3N_4 (10 wt.%), CDs/g-C_3N_4 (50 wt.%) and CDs/g-C_3N_4 (100 wt.%), respectively; (**b**) MoO_3, g-C_3N_4, CM3 and 0.5CCM3 (reproduced with permission from [92,100]. Copyright Royal Society of Chemistry, 2017; Elsevier, 2018; respectively).

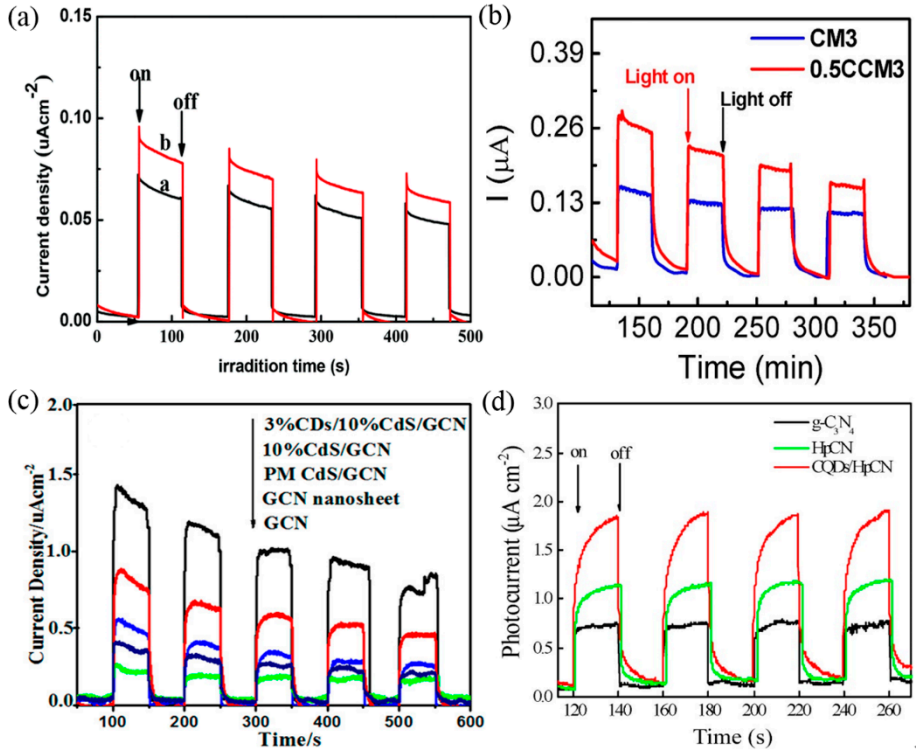

Figure 5. Transient photocurrent responses of (**a**) g-C_3N_4 and CDs/g-C_3N_4 (10 wt.%), (**b**) CM3 and 0.5CCM3, (**c**) GCN, GCN nanosheet, PM CdS/GCN, 10%CdS/GCN and 3%CDs/10%CdS/GCN, (**d**) g-C_3N_4, HpCN and CQDs/HpCN (reproduced with permission from [92,100,105,106]. Copyright Royal Society of Chemistry, 2017; Elsevier, 2018; American Chemical Society, 2018; Elsevier, 2016; respectively).

2.2. Thermal Polymerization Method

The thermal polymerization method proceeds via the conversion of monomeric precursors into polymers under high temperature conditions, which can enhance the connection between CQDs and g-C_3N_4 because of the hydrogen bonds formed between precursors. Wang et al. [90] synthesized N-doped carbon dots (NCD)/g-C_3N_4 composites through a facile hydrothermal-polymerized method using citric acid, urea, and dicyandiamide as precursors. The loading of NCD reduced the band gap and broadened the UV-vis absorption band. They applied the composite to the degradation of IDM and found that 1.0 wt.% NCD/g-C_3N_4 resulted in a 13.6-fold higher reaction rate than that of pristine g-C_3N_4

under visible light irradiation. Wang et al. [101] synthesized CQD-implanted g-C_3N_4 nanotubes (CCTs) by thermal polymerization of freeze-dried urea and the CQDs precursor, as illustrated in Figure 6. The HRTEM image (Figure 7a) exhibits that many small CQDs were distributed on the constitutive g-C_3N_4, which leads to micro-regional heterostructures between graphite carbon and g-C_3N_4. Additionally, the fast Fourier transform (FFT) pattern in Figure 7b displays a hexagonal crystalline structure of the CQDs. The CCTs could efficiently split water under visible light irradiation with an H_2 production rate up to 3538.3 mmol g^{-1} h^{-1} and a high quantum yield of 10.94% at 420 nm. Wang et al. [102] fabricated CDs/g-C_3N_4 hybrids via in situ thermal polymerization of precursors, urea, and glucose, which resulted in enhanced photocatalytic H_2 evolution activity under visible-light. CN/G0.5 hybrids exhibited good stability and an optimal H_2 evolution rate (2.34 mmol g^{-1} h^{-1}), which was 4.55-fold higher than that of bulk g-C_3N_4 (0.51 mmol g^{-1} h^{-1}). The stacking distance of the layer structure reduced from 0.322 nm to 0.318 nm due to the effect of CDs on the thermal polymerization of urea as depicted by XRD patterns (Figure 8a). The PL spectra showed that the intensity of CN/Gx hybrids were reduced as compared with BCN, which implies the interfacial interactions between CDs and g-C_3N_4 could suppress the recombination of charge carries.

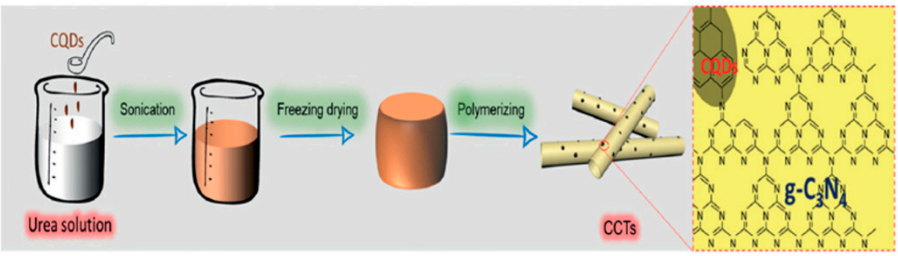

Figure 6. CCTs preparation procedure (reproduced with permission from [101]. Copyright Wiley-VCH, 2018).

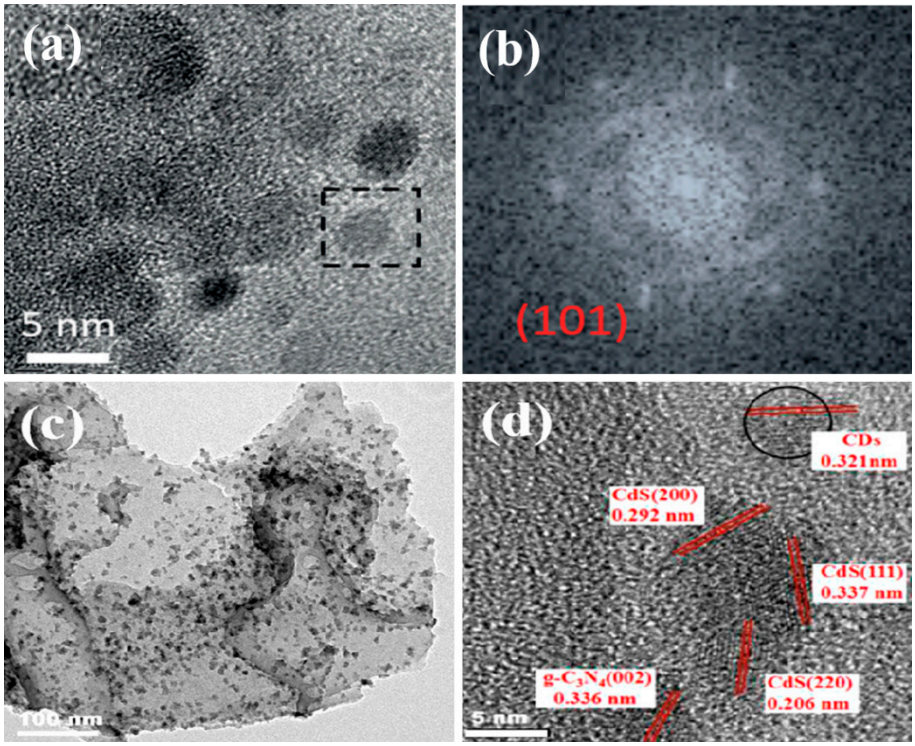

Figure 7. (**a**) HRTEM image of CCTs and (**b**) FFT pattern of the crystallite in (**a**) (reproduced with permission from [101]. Copyright Wiley-VCH, 2018). TEM image (**c**) and HRTEM image (**d**) of 3%CDs/10% CdS/GCN (reproduced with permission from [105]. Copyright American Chemical Society, 2018).

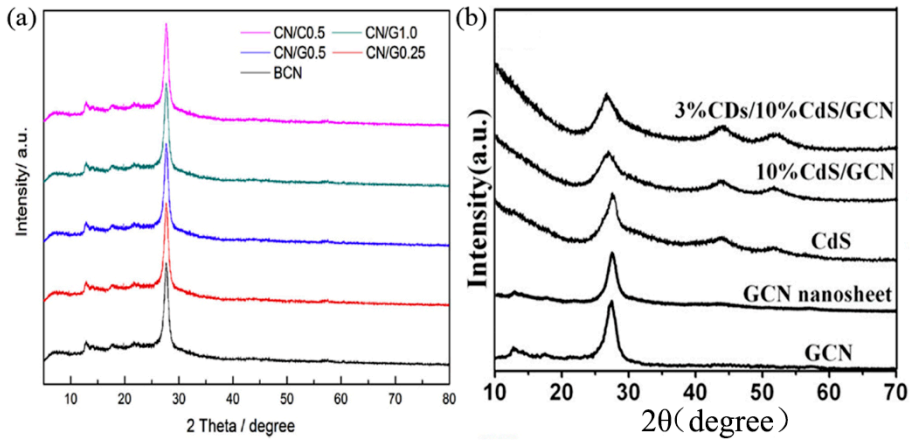

Figure 8. XRD patterns of (**a**) BCN, CN/G0.25, CN/G0.5, CN/G1.0 and CN/C0.5, (**b**) pure GCN, GCN nanosheets, CdS QDs, 10%CdS/GCN and 3%CDs/10%CdS/GCN (reproduced with permission from [102,105]. Copyright American Chemical Society, 2018; Elsevier, 2016; respectively).

2.3. Calcination Method

The calcination method usually occurs at 550 °C under ambient condition for the synthesis of QDs/g-C_3N_4 composites. Liu et al. [20] prepared CQDs/g-C_3N_4 composites by calcinating urea and ammoniated CQDs at 550 °C. CQDs/g-C_3N_4 had a large water-catalyst interface area of 97 m^2 g^{-1}. The Tauc plot curve of CQDs/g-C_3N_4 showed an apparent tail between 2.0 and 2.7 eV, which could improve the light absorbance. The performance of CQDs/g-C_3N_4 for photocatalytic water splitting was evaluated under visible light irradiation. The quantum efficiencies were measured at 16% for wavelength $\lambda = 420 \pm 20$ nm, 6.29% for $\lambda = 58\,0 \pm 15$ nm, and 4.42% for $\lambda = 60\,0 \pm 10$ nm. An overall solar energy conversion efficiency of 2.0% was determined. Fang et al. [93] used a novel method to fabricate CDs/g-C_3N_4 hybrids by calcinating a mixture of CDs and dicyandiamide. The introduction of CDs caused the lattice distortion of the g-C_3N_4, but had little effect on the Brunauer-Emmett-Teller (BET) specific area of g-C_3N_4 and did not improve the light-harvesting ability of g-C_3N_4. The photocatalytic performance of Rhodamine B (Rh B) degradation under UV irradiation and hydrogen production under visible irradiation were studied. The results showed that CDs/g-C_3N_4 displayed excellent photocatalytic activity at 3-fold higher than pristine g-C_3N_4. Xie et al. [100] synthesized a highly efficient CDs/g-C_3N_4/MoO_3 (CCM3) photocatalyst using $(NH_4)_6Mo_7O_{24}{\cdot}4H_2O$, dicyandiamide, citric acid, and urea through a facile calcination method. The SEM image (Figure 9a) shows that the crystalline MoO_3 particles were wrapped in thin amorphous g-C_3N_4 layers. The absorption abilities of 0.5 wt.% CDs/g-C_3N_4/MoO_3 (0.5CCM3) in the visible light region were enhanced significantly due to the presence of CDs, as illustrated in Figure 4b. PL analysis in Figure 10a shows that the emission peak of all samples occurred at ca. 450 nm under an excitation wavelength of 300 nm, and loading CQDs dramatically decreased the PL intensity, which suggested that CDs efficiently improved the separation of photoexcited charge carriers. The photocurrent density of 0.5CCM3 photocatalyst was about 1.5-fold to 2-fold higher than that of CM3, as shown in Figure 5b. Photocatalytic results showed that 0.5CCM3 resulted in 88.4% removal of tetracycline (TC) as compared to 43.2% of MoO_3/g-C_3N_4 composite under the same irradiation conditions.

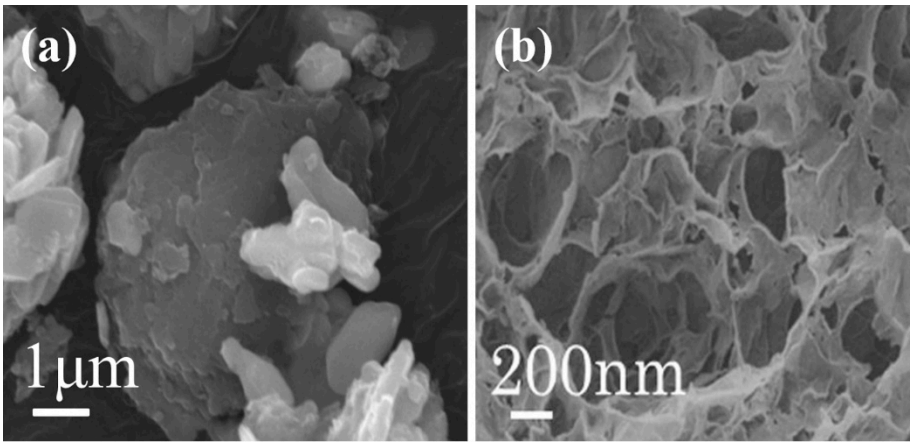

Figure 9. (**a**) SEM image of 0.5CCM3, (**b**) high-magnification FESEM image of GA-CQDs/CNN-24% (reproduced with permission from [100,110]. Copyright Elsevier, 2018; Elsevier, 2018; respectively).

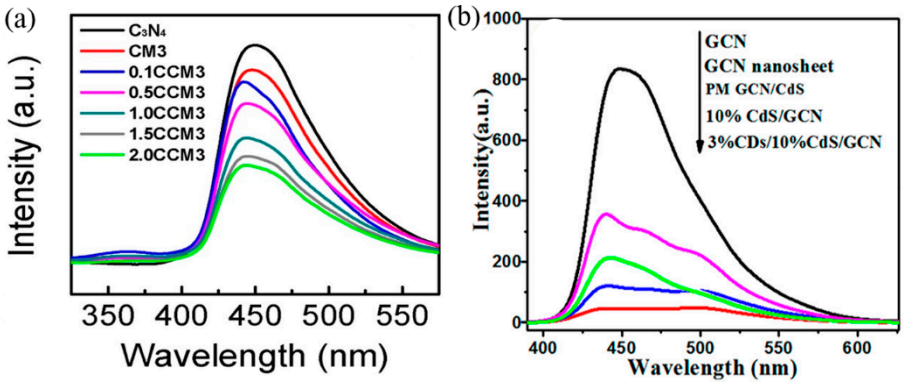

Figure 10. Photoluminescence (PL) emission spectra of (**a**) g-C_3N_4, (1–10%) MoO_3/C_3N_4 composites, and 0.5CCM3 at an excitation wavelength of 300 nm, (**b**) GCN, GCN nanosheets, PM CdS/GCN, 10%CdS/GCN and 3%CDs/10%CdS/GCN at an excitation wavelength of 325 nm (reproduced with permission from [100,105]. Copyright Elsevier, 2018; American Chemical Society, 2018; respectively).

2.4. Solvothermal Method

Using the solvothermal synthesis approach, the use of heat and solvents are combined, with various commonly available solvents employed, such as methanol and ethanol. This method has the advantages of mild reaction conditions, good uniformity, high efficiency, and easy control. Li et al. [103] deposited CQDs onto graphite-like carbon nitride nanosheets (CNNS) to form CNNS/CQDs composites via a facile solvothermal reaction in ethanol. CQDs showed strong optical absorption in the UV region, with a tail extending to the visible range. The PL emission intensity of CNNS/CQDs-7 prepared by adding 90 mg g-C_3N_4 nanosheets into 7 mL CQDs ethanol solution decreased clearly, which suggests that charge recombination was inhibited by loading CQDs. Compared to pure CNNS, light absorption in the UV-vis light region was greatly enhanced by increasing the content of CQDs. After introducing CQDs, the band gap of CNNS decreased from 2.83 eV to 2.80 eV, which enhanced the visible light absorption. The photocatalytic performance of CNNS/CQDs was evaluated based on the photocatalytic production of H_2 under visible light. The highest H_2 production rate was 116.1 μmol h^{-1}, which was two-fold higher than that of pure CNNS (37.8 μmol h^{-1}). Jiang et al. [105] prepared CDs/CdS QDs/g-C_3N_4 (CDs/CdS/GCN) composites through a combination of solvothermal and physical coprecipitation methods. The XRD pattern (Figure 8b) exhibits that the introduction of CDs would not affect the crystal phase and structure of CdS/GCN heterojunctions. The TEM image (Figure 7c) explains CdS QDs and CDs were uniformly loaded on the surface of the GCN nanosheets with less than 10 nm diameters. HRTEM image (Figure 7d) confirms the existence of GCN, CdS

QDs, and CDs, and the close contact among them in 3%CDs/10%CdS/GCN. The PL intensities of the GCN nanosheets, PM CdS/GCN, 10%CdS/GCN, and 3%CDs/10%CdS/GCN decreased, as shown in Figure 10b, which indicated a more efficient separation rate of photogenerated electrons and holes. Photocatalytic activities of the obtained GCN nanosheets and CdS/GCN were evaluated by H_2 evolution reactions under visible-light irradiation in a p-nitrophenol solution. Results showed that 3%CDs/10%CdS/GCN exhibited optimal photocatalytic H_2 evolution efficiency.

2.5. Impregnation Method

Zhang et al. [96] synthesized a CDs/g-C_3N_4 photocatalyst via a facile impregnation-thermal method using cyanamide, citric acid, and ethylenimine as precursors. The PL emission spectra of CDs exhibited an excitation wavelength-dependent behavior due to the existence of different emission states of CDs. CDs enhanced the production of photogenerated electron-hole pairs by absorbing visible light with longer wavelength (550 nm) and then emitted photoluminescence at a shorter wavelength (400–500 nm) due to the upconverted photoluminescence properties. Under visible light irradiation, g-C_3N_4/CDs composites with 0.5 wt.% CDs resulted in a 3.7 times faster reaction rate for phenol photodegradation than pristine g-C_3N_4. Tang et al. [98] used an impregnation method to synthesize a metal-free CQDs/g-C_3N_4 photocatalyst, which significantly enhanced the photocatalytic inactivation of *Staphylococcus aureus* compared with pure g-C_3N_4 in vitro. CQDs/g-C_3N_4 caused a rapid increase in intracellular reactive oxygen species levels and the destruction of cell membranes under visible light, which eventually led to the death of bacteria, while the side effects of CQDs/g-C_3N_4 were negligible. CQDs reduced the band gap of g-C_3N_4 from 2.71 eV to 2.59 eV due to the narrow band gap of CQDs. Furthermore, CQDs/g-C_3N_4 exhibited significantly weakened emission peak intensity and higher photocurrent density as compared with g-C_3N_4, which implies that CQDs could remarkably inhibit the recombination of electron-hole pairs and promote charge-transfer properties.

3. The Property, Applications and Photocatalytic Mechanism of CQDs/g-C_3N_4 Based Photocatalysts

As depicted in Figure 11, many researchers have decorated g-C_3N_4 with CQDs to fabricate metal-free systems, which included binary and ternary photocatalysts and significantly enhanced the photocatalytic performance.

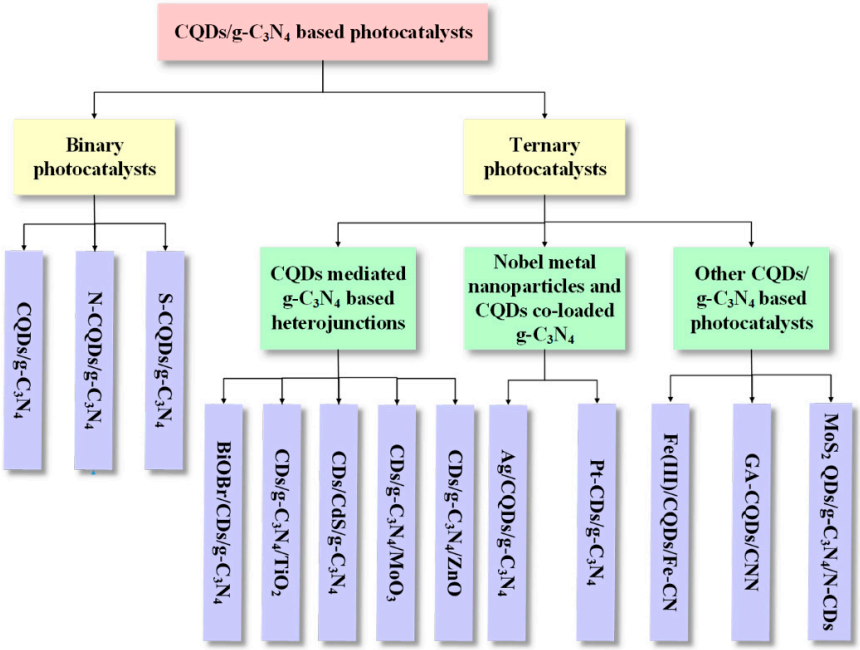

Figure 11. The classification of CQDs/g-C_3N_4-based photocatalysts.

3.1. Binary CQDs/g-C_3N_4 Photocatalysts

3.1.1. CQDs/g-C_3N_4 Photocatalysts

Hong et al. [95] synthesized CQDs/g-C_3N_4 heterojunctions via a facile low temperature process. When CQDs were modified with g-C_3N_4, which possessed absorption wavelength from the UV to about 460 nm, the absorption edges of the CQDs/g-C_3N_4 heterostructures could extend to 400–600 nm. C0.50%/CN degraded 95.2% of Rh B and 78.6% of TC-HCl under visible-light within 3.5 h, and the reaction rate for the photodegradation of Rh B and TC-HCl were about 3.7-fold and 1.9-fold higher than that of bare g-C_3N_4, respectively. Moreover, CQDs/g-C_3N_4 also exhibited excellent photostability and recyclability for both the photodegradation of Rh B and TC-HCl. Feng et al. [97] doped nonpolar CQDs on g-C_3N_4 to construct a CQDs/g-C_3N_4 heterojunction photocatalyst. The narrow band gap of CQDs improved the visible-light absorption and even infrared light absorption. The red shift of the conduction band minimum resulted in a narrower band gap for CQDs/g-C_3N_4 (2.5 eV) compared with that of g-C_3N_4 (2.8 eV). PL spectra showed that the PL emission intensity of CQDs/g-C_3N_4 composites was significantly lower than that of g-C_3N_4, which indicated that CQDs improved the charge-carrier separation efficiency. It was found that CQDs could simultaneously improve the adsorption of nonpolar CO_2 and photo-induced H_2, which enhances reaction kinetics and alters CO_2 photoreduction pathways to generate CH_4. Consequently, in contrast to g-C_3N_4, which only generated CO and H_2, CQDs/g-C_3N_4 could generate 6-fold more CO and comparable levels of CH_4 without any detectable H_2 under the same conditions. No detectable performance deterioration was observed after five repeated cycles of use, which indicates sustained long-term stability of CQDs/g-C_3N_4. Jian et al. [106] developed a novel approach to obtain a CQDs/g-C_3N_4 (CQDs/HpCN) nanocomposite with effective interfacial contact by incorporating negatively charged CQDs and tailor-made proton-functionalized g-C_3N_4 via an electrostatic self-assembly strategy. The dominant peaks in CQDs/HpCN samples showed a slight shift to higher binding energies, which indicated that an electronic interaction between CQDs and HpCN was formed. The incomplete semicircular Nyquist spectrum of CQDs/HpCN modified photoelectrode was characterized with the lowest resistance. Thus, the CQDs/HpCN modified photoelectrode yielded the highest photocurrent, which was much larger than the photocurrent density of pure g-C_3N_4 and HpCN (as shown in Figure 5d). Results showed that CQDs/HpCN exhibited good photocatalytic activity for methylene blue (MB) degradation under visible light irradiation on account of the synergetic interactions between CQDs and HpCN.

In a CQDs/g-C_3N_4 binary system, the improved photocatalytic activity originated from the synergistic interactions between CQDs and g-C_3N_4. First, CQDs act as a photosensitizer, making the g-C_3N_4 absorb more visible light due to its up-converted photoluminescence property [103] and stimulating g-C_3N_4 to produce electron-hole pairs and more reactive $^{\bullet}O_2^-$ and •OH radicals to improve its photocatalytic ability. Second, CQDs act as electron-sinks, which can trap photoexcited electrons and prevent their recombination with photogenerated holes at valence band (VB) in g-C_3N_4 [75]. Third, CQDs/g-C_3N_4 can form a type-II van der Waals heterojunction, which leads to a significant reduction in the band gap [122], and photoexcited electrons effectively migrate from g-C_3N_4 to CQDs via well contacted heterojunction interface, which retards charge recombination [75]. The band alignment in the CQDs/g-C_3N_4 junction can facilitate the separation of photogenerated electron-hole pairs [96].

3.1.2. Nonmetal-Doped CQDs/g-C_3N_4 Photocatalyst

Although CQDs have excellent properties, challenges still exist in the use of the CQDs/g-C_3N_4 photocatalyst, such as the high expense of precursors, rigorous reaction condition requirements, time-consuming purification processes, and low luminescent quantum yield (<10%) [123]. Similar to other nanomaterials, doping heteroatoms into CQDs could create defect levels in the form of recombination centers to alter charge transfer and improve performance [124]. In particular, N-doped CQDs (N-CQDs) have attracted considerable attention because N atoms can improve quantum yield [125], electron transfer, and extend the visible light adsorption region [126]. Currently,

N-CQDs have exhibited unique properties such as electrocatalytic activity, tunable luminescence, and biocompatibility [127,128]. These properties make N-CQDs widely used in photocatalysis, photodetection, and bioimaging [129–133]. Wang et al. [90] synthesized N-doped carbon dots (NCD)/g-C_3N_4 via a polymerization method. Doping NCD remarkably decreased the PL intensity of NCD/g-C_3N_4 compared to g-C_3N_4 and the emission peak of NCD/g-C_3N_4 showed a clear red-shift from 444 nm to 455 nm. Results exhibited that the photocatalytic activity of 1.0 wt.% NCD/g-C_3N_4 was 13.6-fold higher than that of pristine g-C_3N_4 under visible light. Potential photocatalytic mechanisms were proposed in Figure 12. Under visible light irradiation, g-C_3N_4 absorbed <475 nm light to form electron-hole pairs. The >475 nm light was converted to <475 nm light by NCD and absorbed by g-C_3N_4. The CB-level of NCD is lower than that of g-C_3N_4, so the electrons in the CB of g-C_3N_4 can easily transfer to NCD via the heterojunction interface between g-C_3N_4 and NCD, which leads to efficient separation of electron-hole pairs. Molecular O_2 may capture the electrons in NCD to generate $^{\bullet}O_2^{-}$. $^{\bullet}O_2^{-}$ may react with H^+ to generate •OH and react with h^+ to generate O_2. When the VB position of g-C_3N_4 (+1.36 eV) is more negative than the standard redox potential of •OH/OH^- (+1.99 eV) and •OH/H_2O (+2.73 eV), the h^+ from g-C_3N_4 cannot oxidize OH^- or H_2O to generate •OH. Then, the photodegradation of IDM in VB may due to the direct reaction with h^+. Therefore, the efficient degradation of indomethacin (IDM) was contributed to the produced $^{\bullet}O_2^{-}$, h^+, O_2, and •OH.

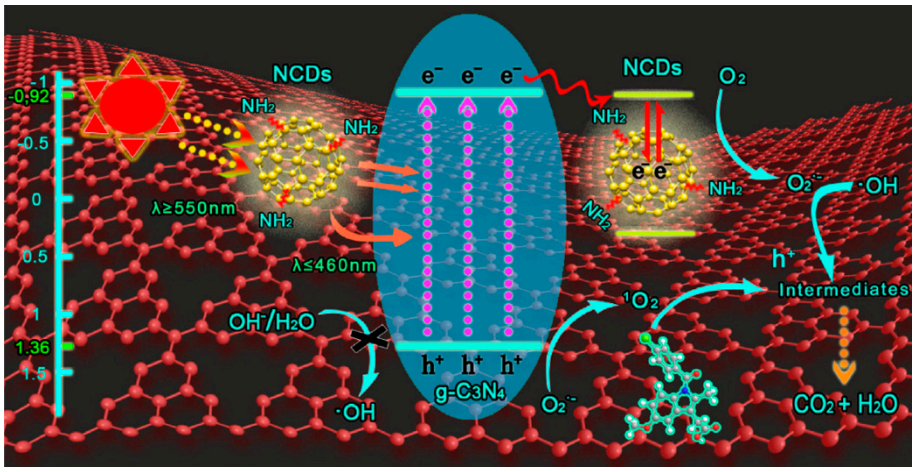

Figure 12. Schematic illustration of the possible photocatalytic processes in NCD/g-C_3N_4 composites (reproduced with permission from [90]. Copyright Elsevier, 2017).

Furthermore, a sulfur doped CQDs (S-CQDs)/hollow tubular g-C_3N_4 photocatalyst (HTCN-C) was fabricated via an ultrasonic assisted method by Wang et al. [104]. Characterization by UV-Vis diffuse reflectance spectra, photoluminescence, transient photocurrent responses, and electrochemical impedance spectroscopy demonstrated good optical and electrochemical properties in samples, which resulted in a significant improvement in photocatalytic efficiency. Doping of HTCN-C(2) with 2 mL S-CQDs solution exhibited optimized performance with a degradation rate of 0.0293 min^{-1} for TC and 99.99% destruction of *Escherichia coli* under visible-light irradiation.

3.2. Ternary CQDs/g-C_3N_4 Based Photocatalysts

3.2.1. CQDs Mediated g-C_3N_4-Based Heterojunction Photocatalysts

It has been reported that combining g-C_3N_4 with other semiconductors to form hetero-structured photocatalysts would efficiently separate photogenerated electrons and holes, enhancing the photocatalytic activity of g-C_3N_4 under visible light irradiation [134–136]. Therefore, many researchers have attempted to introduce CQDs into g-C_3N_4 based heterojunction photocatalysts. Zhang et al. [91] constructed the Z-scheme 2D/2D BiOBr/CDs/g-C_3N_4 heterojunctions, using carbon dots as solid-state

electron mediators. The BiOBr/CDs/g-C_3N_4 hybrids exhibited remarkable interfacial charge transfer abilities and a broadened solar light absorption range due to the short charge transport distance and the up-converted photoluminescence characteristics of CDs. Simultaneously, the enhanced specific surface area and nanosheet structure could provide more active sites to BiOBr/CDs/g-C_3N_4 composites. As a result, BiOBr/CDs/g-C_3N_4 composites significantly enhanced CIP photodegradation under visible light irradiation in comparison to pristine BiOBr nanosheets and g-C_3N_4 ultrathin nanosheets, as depicted in Figure 13a. Moreover, BiOBr/CDs/g-C_3N_4 composites showed excellent photostability and reusability for CIP degradation after 10 repeated cycles, as demonstrated in Figure 13b. Xie et al. [100] constructed a novel CDs modified Z-scheme photocatalyst (CDs/g-C_3N_4/MoO_3), which exhibited remarkably enhanced visible-light photocatalytic activity for the degradation of TC compared to pristine g-C_3N_4 and the MoO_3/g-C_3N_4 composite. Doping with 0.5% CDs showed the highest TC degradation rate, which was 3.5 and 46.2 times higher than that of MoO_3/g-C_3N_4 and g-C_3N_4, respectively. As illustrated in Figure 14, under visible light irradiation, MoO_3 and g-C_3N_4 can efficiently absorb light up-converted by CDs with wavelengths of less than 416 nm and 460 nm. Therefore, the electron-hole pairs were photogenerated on the surface of MoO_3 and g-C_3N_4, respectively. Electrons in the CB of MoO_3 transferred rapidly into the VB of g-C_3N_4 and recombined with holes due to the Z-scheme heterojunctions between MoO_3 and g-C_3N_4, which leads to the accumulation of electrons in the CB of g-C_3N_4 and holes in the VB of MoO_3. The CB of g-C_3N_4 (−1.16 eV) was more negative than $O_2/{}^{\bullet}O_2^-$ (−0.046 eV) and, therefore, electrons on the CB of g-C_3N_4 could react with O_2 to produce ${}^{\bullet}O_2^-$. Similarly, the VB of MoO_3 (3.54 eV) was more positive than •OH/OH^- (+2.27 eV) and it was easy for holes to oxidize OH^-/H_2O to product •OH. These active species could directly degrade TC.

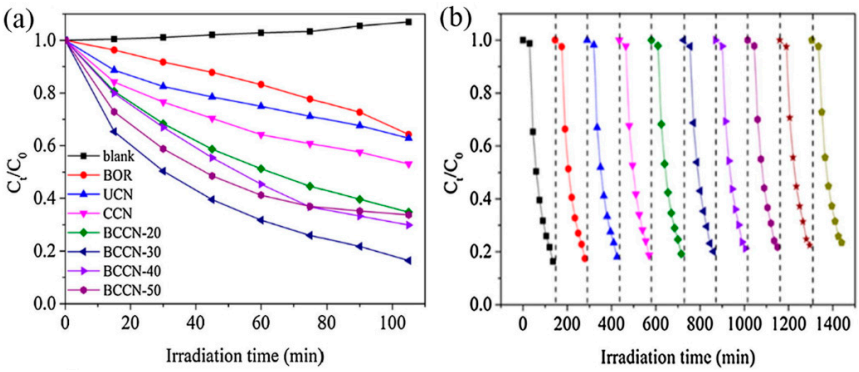

Figure 13. Photocatalytic activity (**a**) and recycling performance (**b**) of BCCN-30 for ciprofloxacin (CIP) degradation under visible-light irradiation (reproduced with permission from [91]. Copyright Elsevier, 2018).

Jiang et al. [105] prepared CDs/CdS QDs/g-C_3N_4 (CDs/CdS/GCN) photocatalysts. The UV-vis diffuse reflectance spectra for 3%CDs/CdS/GCN exhibited optimal absorption intensity in the visible region and marked red-shifts due to the good light absorption property of CDs and CdS QDs. As shown in Figure 5c, 3%CDs/10%CdS/GCN owned the highest photocurrent intensity, which indicated the best efficiency in terms of both interfacial charge transfer and separation of photogenerated electrons and holes. The optimum loading amount of CdS QDs is 10 wt.%, which shows the highest H_2 evolution rate of 9.4 μmol g^{-1} h^{-1} with a 98% 4-NP removal under visible-light irradiation due to the formation of interfaces between CdS QDs and GCN nanosheets, which leads to a high charge separation efficiency. Guo et al. [107] prepared the CDs/g-C_3N_4/ZnO nanocomposite using melamine, $Zn(CH_3COO)_2{\cdot}2H_2O$, and graphite rods as precursors via a facile impregnation-thermal method, which exhibited outstanding photocatalytic activity for the photodegradation of TC. The BET specific surface area of 30 wt.% g-C_3N_4/ZnO (CZ30)-CDs4 was 9.56 m^2 g^{-1} whereas it was 6.38 m^2 g^{-1} for CZ30. The CZ30-CDs4 could degrade almost 100% of TC within 30 min under very weak visible irradiation (λ > 420 nm), which displays the highest activity among all assessed photocatalysts.

The enhanced photocatalytic ability could be ascribed to CDs deposited on the surface of the binary g-C_3N_4/ZnO composite, which absorbed a wider spectrum of visible light and hindered the combination of electron-hole pairs through its excellent electron transfer property. Li et al. [108] prepared a novel ternary layered CDs/g-C_3N_4/TiO_2 nanosheets (CGT) composites by impregnation precipitation methods. TEM images exhibited that the size of CDs were mostly in the diameter range of 10–20 nm with lattice spacing of ca. 0.20 nm. Electron paramagnetic resonance (EPR) spectra showed that the loading of CDs distinctly enhanced peak intensity, which indicated a higher concentration of unpaired electrons for CGT2. Results suggested that the CGT composite revealed a high photocatalytic hydrogen evolution rate in triethanolamine aqueous solutions, which was five times higher than that of the optimal g-C_3N_4/TiO_2 composite.

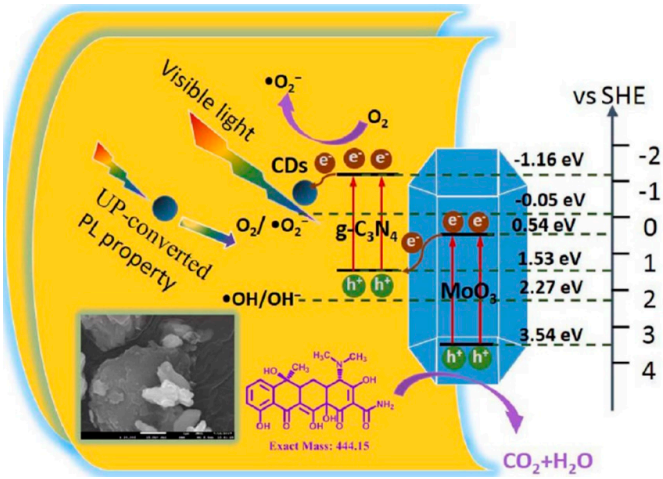

Figure 14. Proposed photocatalytic degradation mechanisms of TC under visible light irradiation with 0.5CCM3 composites (reproduced with permission from [100]. Copyright Elsevier, 2018).

3.2.2. Nobel Metal Nanoparticles and CQDs co-Loaded g-C_3N_4 Photocatalysts

Loading QDs can improve the photocatalytic performance of g-C_3N_4 in hydrogen production and the photodegradation of organic pollutant [137–140], but the recombination rate of photogenerated electrons and holes remains high. To further improve the quantum efficiency and photocatalytic activity of CDs/g-C_3N_4, it is necessary to find suitable semiconductors to couple with CDs/g-C_3N_4. As emerging and promising materials for exploiting visible light efficiently, noble metal atoms (such as gold, silver and platinum) function as suitable co-catalysts in photocatalytic systems, which mainly due to the surface plasmon resonance (SPR) effect of noble metals. The SPR effect can not only enhance the optical absorption in the visible light region [141], but can also promote the photocatalytic formation of electrons and holes. Moreover, noble metals can extend optical path lengths for photons in the photocatalyst by scattering resonant photons efficiently, and then improving the evolution rates of charge carriers [142]. Noble metals can also act as electron sinks similarly to CQDs and capture electrons, impeding the recombination of electron-hole pairs.

Qin and Zeng [89] designed Ag NPs/CQDs/g-C_3N_4 complex photocatalysts by a facile method using glucose, urea and $AgNO_3$ as precursors. The photocatalytic hydrogen production activity of the catalysts were evaluated, as depicted in Figure 15a, showing that the 3 wt.% Ag/CQDs/g-C_3N_4 hybrid system possessed the highest photocatalytic HER of up to 626.93 μmol g^{-1} h^{-1} under visible light. This was 6.7-fold and 2.8-fold higher than pure g-C_3N_4 and the optimal CQDs/g-C_3N_4 composite, respectively. The charge generation and transfer procedure of the Ag/CQDs/g-C_3N_4 composite combined with conjectural photocatalytic H_2 evolution mechanism are illustrated in Figure 16. Under sunlight irradiation, g-C_3N_4 could only absorb light at wavelengths of less than 460 nm, while photogenerated electrons help the Ag/CQDs/g-C_3N_4 system to capture photons with wavelengths shorter than 550 nm due to the SPR effect of Ag. At the same time, longer wavelengths of more

than 550 nm were up-converted to shorter wavelengths by CQDs. All these factors increased the absorption of sunlight by Ag/CQDs/g-C_3N_4 and facilitated high-efficiency photoelectrons generation, transfer, and separation. In addition, the photoelectrons could rapidly migrate to CQDs and Ag NPs through the junction interface due to the matched band alignment [143,144]. Then, photoelectrons in the CB of g-C_3N_4 were available for H^+ reduction to emit H_2 [145]. Furthermore, as shown in Figure 15b, there was no clear difference in catalytic effect after four cycles of reuse under visible light illumination. Wang et al. [100] prepared Pt-CDs/g-C_3N_4 photocatalysts using a Pt co-catalyst via a photoreduction approach. TEM images exhibit that Pt nanoparticles with a uniform diameter of ca. 2 nm were homogeneously distributed on the surface of carbon dots or g-C_3N_4. They evaluated the photocatalytic performance of photocatalysts and found that Pt-CDs/g-C_3N_4 (10 wt.%) showed the highest H_2 production, which was 2.1-fold more than for Pt/g-C_3N_4 under UV-light irradiation. Pt-CDs/g-C_3N_4 (10 wt.%) also exhibited the highest H_2 production rate under visible-light irradiation as well as being capable of splitting pure water to produce H_2.

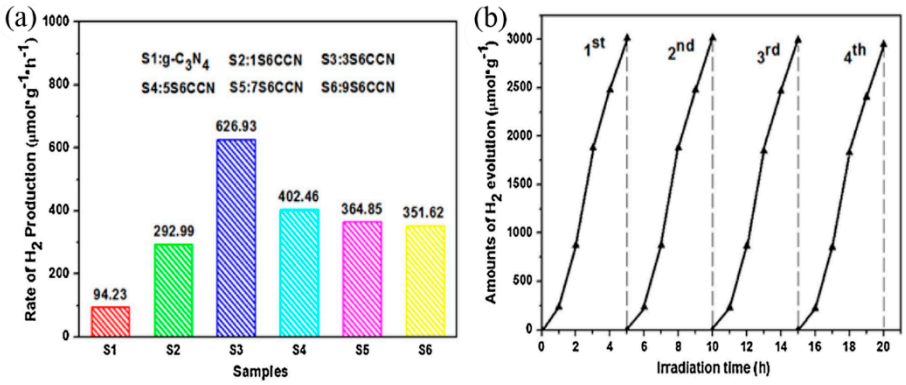

Figure 15. (**a**) Photocatalytic activity of pure g-C_3N_4 and Ag NPs modified 6CCN (6 mL CQDs/g-C_3N_4) composites with different contents for photocatalytic H_2 generation under visible-light irradiation, (**b**) Recycling performance of 3S6CCN towards photocatalytic H_2 generation (reproduced with permission from [89]. Copyright Elsevier, 2017).

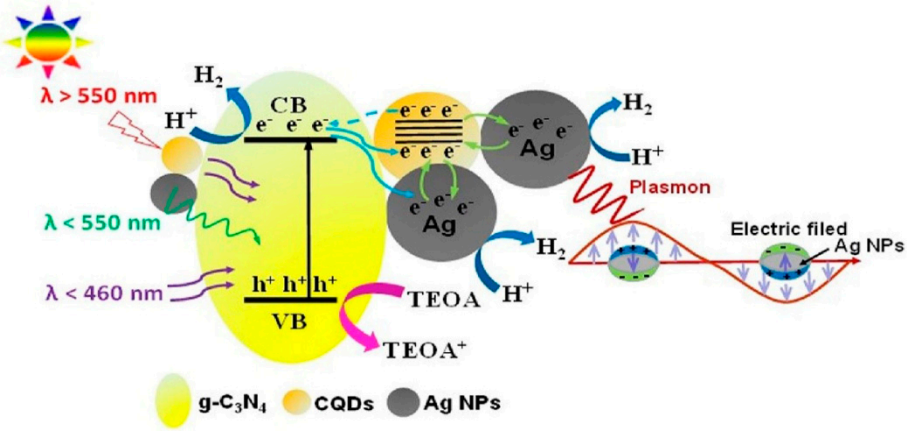

Figure 16. Schematic illustration of the charge generation and transfer procedure of the Ag/CQDs/g-C_3N_4 composite combined with a conjectural photocatalytic H_2 evolution mechanism (reproduced with permission from [89]. Copyright Elsevier, 2017).

3.2.3. Other Ternary CQDs/g-C_3N_4-Based Photocatalysts

Liu et al. [109] synthesized Fe(III)/CQDs/Fe-doped g-C_3N_4 (Fe-CN) binary composite via a facile impregnation method. The obtained composite exhibited an increased specific surface area of 17.51 m^2 g^{-1}, which was 2.06-fold greater than of pure CN, and the pore volume of Fe(III)/CQDs/Fe-CN

was the largest. After incorporation of Fe(III) into Fe-CN, the absorption edge of Fe(III)/Fe-CN exhibited a distinct red shift and the light absorption intensity was enhanced over the whole visible light region. Results showed that photocatalytic activity increased with an increase in the nominal mass fraction of Fe from 2% to 8%, which exhibits that 8% Fe(III)/CQDs/Fe-CN could remove 93% of Methyl Orange (MO) within 60 min under visible light irradiation. This effect was ascribed to the largely promoted light absorption, the reduced transportation distance of photo-induced carriers by the interfacial charge transfer effect, and the generation of •OH active species by the photo-Fenton reaction originating from grafting of Fe(III). He et al. [110] synthesized a new type of three-dimensional (3D) ternary graphene-CQDs/g-C_3N_4 nanosheet (GA-CQDs/CNN) aerogel visible-light-driven photocatalyst via a two-step hydrothermal method. The FESEM image (Figure 9b) depicts that GA-CQDs/CNN-24% possessed a highly interconnected 3D porous structure formed by GO and the diameter ranged from 50 to 500 nm. Therefore, the BET surface areas of GA-CQDs/CNN-24% were larger than that of CNN and CQDs/CNN. The incorporation of CQDs and GA into CNN led to an enhancement of visible light absorption. GA-CQDs/CNN-24% showed the highest photocurrent intensity (0.8 μA cm^{-2}), which was 1.78, 2.29, and 2.50 times higher than that of CQDs/CNN, CNN, and BCN, respectively. The MO removal ratio of GA-CQDs/CNN-24% reached 91.1%, which was 7.6-fold higher than that of bulk g-C_3N_4 under the same conditions. The enhanced photocatalytic performance was attributed to that both CQDs and rGO, which can act as a supporter for the 3D framework that could improve the visible light absorption and promote charge separation.

4. GQDs/g-C_3N_4 Based Photocatalysts

As a novel type of QDs with sizes usually less than 10 nm, GQDs comprise single or multiple layer graphene and have attracted attention in the fields of electrochemical biosensors, energy conversion, bioimaging, and drug delivery on account of its unique edge effects and quantum confinement [146–149]. Therefore, GQDs were widely used as light absorbers to couple with semiconductors [97].

Xu et al. [150] formed unique s-g-C_3N_4@GQD nanohybrids using a rationally designed strategy to assemble ox-GQDs onto s-g-C_3N_4 nanosheets by a one-step hydrothermal treatment. The TEM image of s-g-C_3N_4@GQDs revealed a nanojunction structure with nanosheets cross-linking together and a nanopore structure. The CV curve for s-g-C_3N_4@GQDs exhibited a typical capacitive behavior with an overall larger response current than that of GQDs and the original s-g-C_3N_4. This indicates the presence of more active sites as well as efficient charge separation and transfer channels within s-g-C_3N_4@GQDs. The ORR diffusion current density of s-g-C_3N_4@GQDs was the highest, which reached the potential of the Pt/C electrode. This indicates the high electrochemical activity. Therefore, nanohybrids exhibited remarkably enhanced catalytic activity in the oxygen reduction reaction compared to the original s-g-C_3N_4 and GQDs. Xu et al. [111] constructed ternary graphitic carbon nitride/zinc tetracarboxyphthalocyanine/graphene quantum dots (g-C_3N_4/ZnTcPc/GQDs) through chemical bonding and hydrothermal methods. The addition of GQDs in g-C_3N_4/ZnTcPc/0.1GQDs shifted the C-NH_2 peak from 286.0 eV to 285.7 eV and elevated the C-C peak in comparison with the C-NH_2 peak, as shown in XPS spectra (Figure 17a,b). The g-C_3N_4/ZnTcPc/0.1GQDs composites exhibited increased photocatalytic activity under solar light irradiation. Results showed that the removal rate of Rh B exceeded 98.2%, which was 2-fold higher than that of pure g-C_3N_4. Furthermore, g-C_3N_4/ZnTcPc/0.1GQDs also exhibited a better photocatalytic activity with removal of 63% sulfaquinoxaline sodium within 40 min and 59% carbamazepine within 180 min. Yuan et al. [112] fabricated a metal-free composite photocatalyst of graphene quantum dots modified graphitic carbon nitride nanorods (GQDs/g-CNNR). Characterizations of physicochemical properties indicated that GQDs/g-CNNR photocatalyst exhibited a high crystallization level, enhanced visible light absorption, and staggered band alignment, which improved the photocatalytic activity of GQDs/g-CNNR for the efficient removal of antibiotics. The photocatalytic reaction rate of GQDs/g-CNNR was 3.46-fold and 2.03-fold higher than that of pristine g-C_3N_4 and g-CNNR, respectively.

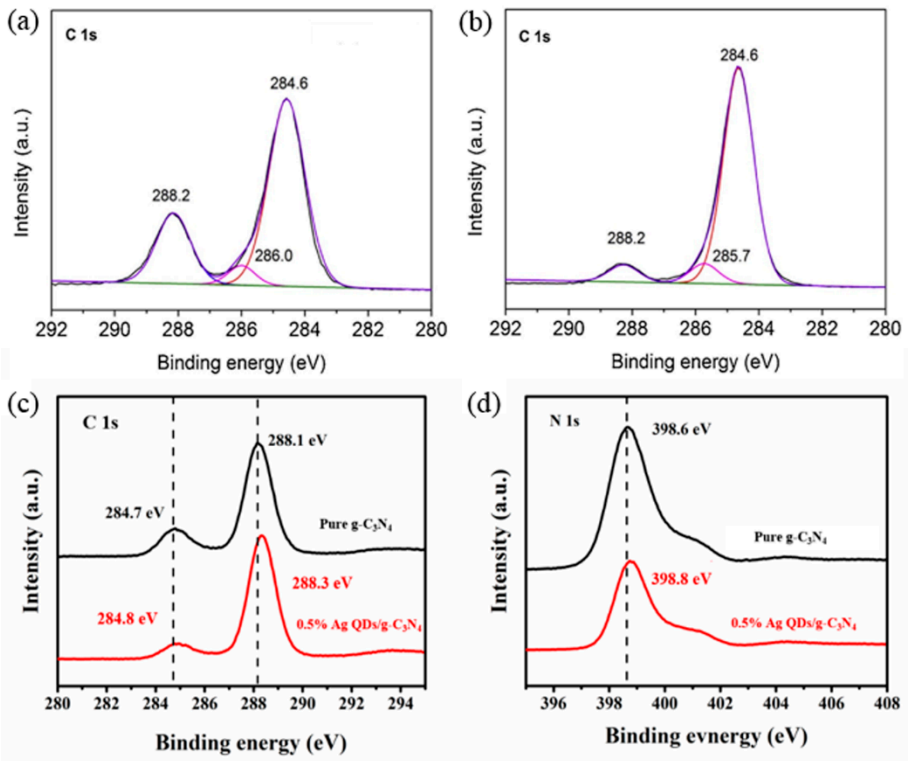

Figure 17. XPS spectra of (**a**) C 1s of g-C_3N_4/ZnTcPc, (**b**) C 1s of g-C_3N_4/ZnTcPc/0.1GQDs (reproduced with permission from [111]. Copyright Elsevier, 2019). XPS spectra of (**c**) C 1s of pure g-C_3N_4 and AX = 0.5% sample, (**d**) N 1s of pure g-C_3N_4 and AX = 0.5% sample (reproduced with permission from [117] Copyright Elsevier, 2016).

Meanwhile, it was reported that N atoms introduced into GQDs (N-GQDs) can serve as photosensitizers to capture visible and NIR light, efficiently promote optical and electron transfer properties, and improve the photocatalytic activity of other photocatalysts. Deng et al. [151] synthesized ternary Ag NPs/N-GQDs/g-C_3N_4 nanocomposites. After coating Ag on the surface of GCN-3 for the formation of AGCN-4, the SSA of AGCN-4 increased from 64.99 to 76.67 m^2/g, while the pore volume decreased from 0.35 to 0.31 cm^3/g. The band gap of AGCN-4 reduced from 2.79 to 2.74 eV, which might facilitate the absorption of more visible light and NIR light. Results indicated that 0.5% N-GQDs and 2.0% AGCN-4 could degrade 92.8% and 31.3% TC under full-spectrum light and NIR light irradiation, respectively, which was three-fold greater than that of pristine g-C_3N_4. The enhanced photocatalytic activity contributed to the synergistic effects among g-C_3N_4, N-GQDs, and Ag NPs. Feng et al. [152] fabricated the N-doped graphene QDs (N-GQDs) modified Ag_2CrO_4@g-C_3N_4 core-shell structured composite (AN@CN), which achieved a full-spectrum response from the UV to the NIR region. The XRD and EIS results confirmed the stable nature of AN@CN composites. In the AN@CN composites, Ag_2CrO_4 and g-C_3N_4 could be excited by UV and visible light, with N-GQDs greatly enhancing the utilization of solar light and effectively promoting photoelectron transfer from Ag_2CrO_4 to g-C_3N_4, which not only restrained charge combination, but also greatly inhibited the photo-corrosion of Ag_2CrO_4. Moreover, the core-shell structure provided a larger contact area between Ag_2CrO_4 and g-C_3N_4 compared with normal hybrid heterojunctions. Thus, AN@CN exhibited excellent photocatalytic degradation of doxycycline under full-spectrum light.

5. g-C_3N_4 QDs/g-C_3N_4-Based Photocatalysts

Constructing g-C_3N_4-based heterojunction photocatalysts has attracted more attention recently. However, the requirement for energy level matching of the two semiconductors limits its widespread development [153] and remarkable differences in physicochemical properties of two semiconductors

may significantly influence the homogeneity, stability, and compatibility of heterojunctions. To overcome these shortcomings, a large effort has been made to construct isotype heterojunctions. Due to their similar molecular and crystalline structures, the hetero-interfaces between two kinds of g-C_3N_4 are natively compatible and enable an internal electric field, which promotes the efficient separation of charge carriers [154].

Wang et al. [113] used a hydrothermal method to construct g-C_3N_4/BCNQDs heterojunctions by modifying g-C_3N_4 with B doped g-C_3N_4 QDs (BCNQDs). A smaller resistance of the incomplete Nyquist plot of g-C_3N_4/BCNQDs formed with 7mL BCNQD (Figure 18a) indicated a more facilitated interfacial transfer of electrons and more efficient separation of photo-generated charge carriers. The g-C_3N_4/BCNQDs heterojunction exhibited an enhanced hydrogen evolution performance for water splitting under visible light irradiation, which contributed to the formation of heterojunctions between g-C_3N_4 and BCNQDs with well-matched band structures. Wang et al. [114] prepared a novel Sb_2S_3/ultrathin g-C_3N_4 sheets heterostructure embedded with g-C_3N_4 QDs (CNS) via a hydrothermal process. Characterization of physicochemical properties demonstrated that the composites exhibited fast electron transport and enhanced solar light absorption. Under NIR irradiation, the MO photodegradation rate of the optimal CNS was 0.0103 min^{-1}, which was 2.6 times higher than that of pure Sb_2S_3. The improved NIR photocatalytic activity may benefit from improved absorption in the NIR region, efficient electron-hole separation, and the up-converted PL property of g-C_3N_4 QDs. Zhang et al. [154] polymerized urea and DCDA into carbon nitrides nanosheets (U-CN) and carbon nitrides particles (D-CN) via different condensation processes to construct an isotype heterojunction. After coupling D-CN particles (containing 1% DCDA) with U-CN nanosheets, the HER gradually increased to a maximum value of 553 mmol h^{-1} g^{-1}, which was 17 and 5 times more than individual D-CN and U-CN, respectively. Zhou et al. [155] reported the formation of g-C_3N_4 QDs (CNQDs) modified g-C_3N_4 (CNQDs/CN), prepared by a simple solvothermal method. HRTEM images show that the average diameter of CNQDs was 3 nm and that CNQDs were uniformly distributed on the surface of bulk g-C_3N_4, while no agglomeration occurred, which might provide more active sites. CNQDs/CN-20 exhibited the weakest PL intensity. Results confirmed that the CNQDs/CN-20 composite could almost completely degrade Rh B within 40 min. The enhanced photocatalytic performance of CNQDs/CN could be ascribed to the effective charge separation and transfer across the interfaces between g-C_3N_4 and CNQDs, which results in the excellent photoelectrochemical properties and prolonged lifetime of charge carriers.

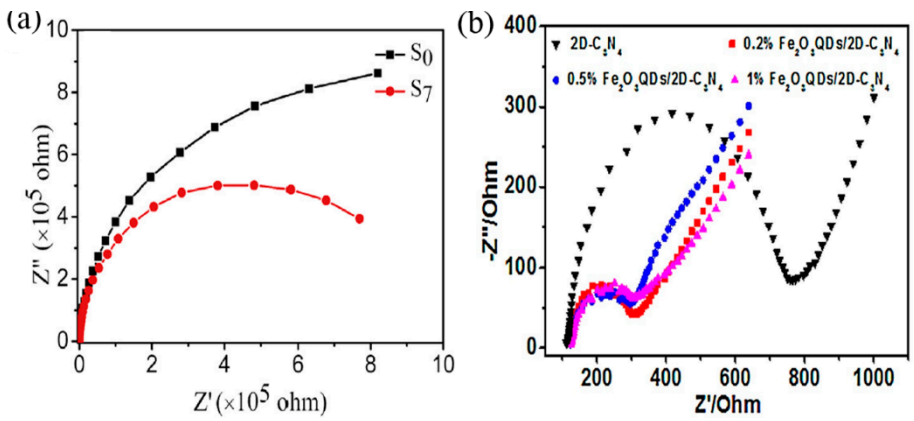

Figure 18. EIS Nyquist plots of (**a**) S_0 and S_7 samples, (**b**) 2D-C_3N_4, 0.2% Fe_2O_3 QDs/2D-C_3N_4, 0.5% Fe_2O_3 QDs/2D-C_3N_4 and 1% Fe_2O_3 QDs/2D-C_3N_4 (reproduced with permission from [113,120]. Copyright Elsevier, 2018; Elsevier, 2018; respectively).

6. Other QDs/g-C_3N_4 Based Photocatalysts

In addition to the previously mentioned photocatalysts, many other types of QDs/g-C_3N_4-based photocatalysts have been synthesized and utilized in various fields. CdS QDs have unique properties and adjustable band gaps, which makes them widely applicable to water pollution treatment and H_2 production [156,157]. However, it is difficult to control the shape of high quality homogeneous and stable semiconductor QDs using traditional solution chemistry [158,159]. One of the most efficient routes to solve this problem is to load CdS QDs onto g-C_3N_4 to form stable nanocomposites [160]. Zhao et al. [115] synthetized O-doped MoS_2 nanospheres/CdS QDs/g-C_3N_4 nanosheets (MoS_2/CdS/g-C_3N_4) through hydrothermal and chemical bath deposition-calcination processes. TEM image displayed that CdS QDs were attached to the surface of MoS_2 nanospheres and that MoS_2 nanospheres were coated with g-C_3N_4 nanosheets. UV-vis diffuse reflectance spectra exhibited that the MoS_2/CdS/g-C_3N_4 composite was capable of optical absorption in both the visible region and the infrared region. MoS_2/CdS/g-C_3N_4 photocatalysts showed the most efficient photocatalytic H_2 evolution. The photodegradation rate of Rh B and bisphenol A (BPA) for MoS_2/CdS/g-C_3N_4 was 99% and 95.2%, respectively. Zheng et al. [160] introduced CdS QDs onto the exterior surface of hollow carbon nitride spheres (HCNS) to synthesize hybrid nano-heterojunctions via an interface self-assembly method. CdS QDs increased the specific surface area of HCNS. The photocatalytic activities of different hetero-structural samples were evaluated for H_2 production. Results showed that 20 wt.% CdS QDs/HCNS exhibited an optimum HER of 601 μmol h^{-1}, which was five times faster than that of non-modified material. The enhanced photocatalytic performance of the heterostructure could be attributed to the unique 3D hollow architectural framework of HCNS, which could serve as a polymeric scaffold to form intimate interfacial contact with CdS QDs to facilitate the surface kinetics of charge separation and mass transfer.

Chen et al. [116] fabricated Bi_2WO_6 QDs/g-C_3N_4 binary heterojunction photocatalysts via a one-pot hydrothermal strategy. The N_2 adsorption-desorption experiment revealed a decreased surface area of BWCN10 (5.6 m^2 g^{-1}) compared to 11.2 m^2 g^{-1} for Bi_2WO_6 QDs. The reduced surface area was attributed to the in-situ deposition of Bi_2WO_6 QDs into the porous structure of ultrathin g-C_3N_4 nanosheets and the formation of large mesopores and macropores. FT-IR spectra exhibited that the characteristic peak from the s-triazinering vibration of g-C_3N_4 nanosheets exhibited a clear blue shift after coupling with Bi_2WO_6 QDs, which indicated that some interactions occurred between g-C_3N_4 and Bi_2WO_6 QDs. The Bi_2WO_6 QDs/g-C_3N_4 composites exhibited clearly enhanced photocatalytic efficiency, which originated from the formation of an internal electric field induced by the enhanced separation efficiency of photogenerated electrons and holes because of the close heterogeneous interface and well-matched band structure. Chen et al. [117] used a novel one-step method to synthesize Ag QDs/g-C_3N_4 photocatalysts, which exhibited high photoactivity for hydrogen production under visible-light irradiation ($\lambda > 420$ nm). The hydrogen production efficiency of 0.5% Ag QDs/g-C_3N_4 reached 18.09 μmol g^{-1} h^{-1}, which was enhanced 4.6 times compared to pure g-C_3N_4. XPS spectras (Figure 17c,d) show that the C 1s and N 1s binding energies had slightly shifted toward a higher binding energy compared to the pure g-C_3N_4, which was ascribed to the strong interfacial interaction between the Ag QDs and g-C_3N_4. UV-vis results demonstrated that the coupled Ag QDs enhanced light absorption in the visible region. In comparison with pure g-C_3N_4, the intensity of the PL signal for 0.5% Ag QDs/g-C_3N_4 decreased markedly, which indicated suppression in the recombination process of electron-holes and enhanced photocatalytic activity of Ag QDs/g-C_3N_4 photocatalysts. Han et al. [118] synthesized black phosphorus quantum dots (BP)@g-C_3N_4 composites via a simple electrostatic attraction approach via the interaction of BP QDs with g-C_3N_4 occurring via P-N coordinate bonding. After loading BP QDs on g-C_3N_4, the absorption band edge of g-C_3N_4 did not change significantly, which suggested that BP QDs did not improve the photon absorption efficiency. BP@g-C_3N_4 exhibited a higher photo-current response and smaller resistance of the incomplete Nyquist arc than g-C_3N_4, which indicated that BP QDs enhanced the light absorption, electron transfer, and carrier separation efficiency of g-C_3N_4. The BP@g-C_3N_4 composites displayed improved carrier separation efficiency

and higher activities for photocatalytic CO_2 reduction to CO (6.54 μmol g^{-1} h^{-1} when loading 1 wt.% BP QDs) in comparison to pure g-C_3N_4 (2.65 μmol g^{-1} h^{-1}) under UV-vis light.

Ye et al. [119] synthesized 0D/2D heterojunctions of vanadate ($AgVO_3$, $BiVO_4$, $InVO_4$, and CuV_2O_6) QDs/g-C_3N_4 NSs via an in-situ growth strategy. Vanadate QDs reduced the band gap of g-C_3N_4 NSs and exhibited a substantial absorption capacity in the visible-light region. The heterojunctions exhibited excellent visible light-driven catalytic activity in organic dye degradation due to the photoactive contribution, up-conversion absorption, and nitrogen coordinating sites of g-C_3N_4 NSs, which resulted in highly dispersed vanadate nanocrystals, strong coupling, and band alignment. Hao et al. [120] formed a 0D/2D Fe_2O_3 QDs/g-C_3N_4 composite using melamine and $Fe(NO_3)_3{\cdot}9H_2O$ by combining ultrasonic dispersion with low temperature calcination. The PL maximum emission peak spectrum exhibited a slight blue shift, which was attributed to a Fe_2O_3 QDs quantum-sized confinement effect. The 0.5% Fe_2O_3 QDs/2D-C_3N_4 photocatalyst has the lowest resistance of the incomplete Nyquist arc radius in Figure 18b, which suggested that it has a superior electron-transfer rate. The decreased arc radius of Nyquist plots for Fe_2O_3 QDs/2D-C_3N_4 composites suggested a smaller charge transfer resistance than that of 2D-C_3N_4. The 0.5% Fe_2O_3 QDs/2D-C_3N_4 composite exhibited the highest photocatalytic activity, which degrades about 75% MB within 180 min under visible light. Zhang et al. [121] used a facile annealing process to fabricate Co_3O_4 QDs/g-C_3N_4 nanosheets. The N_2 adsorption-desorption isotherms depicted specific BET surface areas to be 86.7 m^2 g^{-1} for 0.8% Co_3O_4-C_3N_4-300 whereas 54.5 m^2 g^{-1} for pristine g-C_3N_4 and an increased pore volume to be 0.31 cm^{-3} g^{-1} for 0.8% Co_3O_4-C_3N_4-300 whereas 0.19 cm^{-3} g^{-1} for pristine g-C_3N_4. The flat band potential values of g-C_3N_4 and 0.8% Co_3O_4-C_3N_4 (180, 250, 300) were −0.91, −0.92, −0.87 and −0.74V, respectively, which shows the weakest upward band alignment of g-C_3N_4 and demonstrates an electric field formed at the interface between g-C_3N_4 and Co_3O_4. This could elevate the efficiency of hole transport from g-C_3N_4 to Co_3O_4. Results showed that 0.8% Co_3O_4-C_3N_4-300 obtained the highest O_2 production rate, which was four times higher than that of pristine g-C_3N_4.

7. Summary and Perspectives

In conclusion, g-C_3N_4 has attracted considerable scientific attention due to its high thermal and chemical stabilities as well as unique electronic, optical, and photoelectric properties. Furthermore, as a stabilizer, g-C_3N_4 can improve the durability and stability of loaded materials. In order to optimize the photocatalytic activity of g-C_3N_4, more researchers have attempted to modify g-C_3N_4 with QDs, which can effectively capture photogenerated electrons in g-C_3N_4. However, research efforts in the area of QDs/g-C_3N_4-based photocatalysts remain in their infancy. Many challenges need to be solved in future studies. Therefore, the aspects that warrant further research for the effective application of QDs modified g-C_3N_4-based photocatalysts are proposed.

It is important to develop more effective, facile, economic, and environmentally-friendly synthetic methods to synthesize QDs/g-C_3N_4. In terms of choosing QDs, ideal QDs should have narrow particle size distributions, high fluorescence quantum yield, high stability, non-toxicity, and low cost. Developing efficient methods to load QDs on g-C_3N_4-based photocatalysts and to improve the recyclability of QDs/g-C_3N_4-based photocatalysts are also important. Novel insights are required to create highly effective g-C_3N_4 based photocatalysts to address energy and environmental issues. First, various morphologies such as 0D g-C_3N_4 QDs, nanofibers, nanotubes, nanorods, nanosheets, nanospheres, and mesoporous structures of g-C_3N_4 must be explored to achieve higher surface areas. In addition, improving the photocatalytic performance through hybridization (doping N, O, S), or changing the particle size and loading amount of QDs ought to be explored. Future work requires comprehensive and accurate understanding of the relationship between the structure and properties of QDs/g-C_3N_4-based photocatalysts as well as the dynamics and pathways of charge carrier transfer. Yet, more attention should be paid to the analysis of photodegradation products to avoid producing more harmful secondary pollutants. Attempts should be made to apply QDs/g-C_3N_4-based photocatalysts in more fields such as the preparation of solar cells and sensors. It is expected that this review will provide

readers with a broad view of QDs applications and to promote their further use and development to cope with energy shortages and environmental pollution.

Author Contributions: Y.C. contributed to statistical analysis and manuscript preparation. X.B. contributed to manuscript design and revision. All authors have read and agreed to the published version of the manuscript.

Funding: The authors gratefully acknowledge the support provided by the National Natural Science Foundation of China (Grant No. 21876044), the Outstanding Youth Fund of Jiangsu province (Grant No. BK20170098), and a project funded by the Priority Academic Program Development of Jiangsu Higher Education Institutions.

Conflicts of Interest: The authors declare no conflict of interest.

References

1. Hua, L.; Chen, H.; Wagner, M.J.; Zhang, W.; Shuai, D. Visible-light responsive graphitic carbon nitride: Rational design and photocatalytic applications for water treatment. *Environ. Sci. Technol.* **2016**, *50*, 12938–12948.
2. Fang, X.Z.; Shang, Q.C.; Wang, Y.; Jiao, L.; Yao, T.; Li, Y.F.; Zhang, Q.; Luo, Y.; Jiang, H.L. Single Pt atoms confined into a metal-organic framework for efficient photocatalysis. *Adv. Mater.* **2018**, *30*, 1705112. [CrossRef]
3. Huang, Y.; Liang, Y.; Rao, Y.; Zhu, D.; Cao, J.J.; Shen, Z.; Ho, W.; Lee, S.C. Environment-friendly carbon quantum dots/$ZnFe_2O_4$ photocatalysts: Characterization, biocompatibility, and mechanisms for NO removal. *Environ. Sci. Technol.* **2017**, *51*, 2924–2933. [CrossRef] [PubMed]
4. Zou, Z.; Ye, J.; Sayama, K.; Arakawa, H. Direct splitting of water under visible light irradiation with an oxide semiconductor photocatalyst. *Nature* **2001**, *414*, 625–627. [CrossRef] [PubMed]
5. Hoffmann, M.R.; Martin, S.T.; Choi, W.; Bahnemann, D.W. Environmental applications of semiconductor photocatalysis. *Chem. Rev.* **1995**, *95*, 69–96. [CrossRef]
6. Teoh, W.Y.; Scott, J.A.; Amal, R. Progress in heterogeneous photocatalysis: From classical radical chemistry to engineering nanomaterials and solar reactors. *J. Phys. Chem. Lett.* **2012**, *3*, 629–639. [CrossRef]
7. Huang, D.; Wang, X.; Zhang, C.; Zeng, G.; Peng, Z.; Zhou, J.; Cheng, M.; Wang, R.; Hu, Z.; Qin, X. Sorptive removal of ionizable antibiotic sulfamethazine from aqueous solution by graphene oxide-coated biochar nanocomposites: Influencing factors and mechanism. *Chemosphere* **2017**, *186*, 414–421. [CrossRef]
8. Huang, D.L.; Guo, X.Y.; Peng, Z.W.; Zeng, G.M.; Xu, P.; Gong, X.M.; Deng, R.; Xue, W.J.; Wang, R.Z.; Yi, H. White rot fungi and advanced combined biotechnology with nanomaterials: Promising tools for endocrine-disrupting compounds biotransformation. *Crit. Rev. Biotechnol.* **2018**, *38*, 671–689. [CrossRef]
9. Gong, X.; Huang, D.; Liu, Y.; Peng, Z.; Zeng, G.; Xu, P.; Cheng, M.; Wang, R.; Wan, J. Remediation of contaminated soils by biotechnology with nanomaterials: Bio-behavior, applications, and perspectives. *Crit. Rev. Biotechnol.* **2018**, *38*, 455–468. [CrossRef]
10. Huang, D.L.; Wang, Y.; Zhang, C.; Zeng, G.M.; Lai, C.; Wan, J.; Qin, L.; Zeng, Y. Influence of morphological and chemical features of biochar on hydrogen peroxide activation: Implications on sulfamethazine degradation. *RSC Adv.* **2016**, *6*, 73186–73196. [CrossRef]
11. Pan, J.Q.; Sheng, Y.Z.; Zhang, J.X.; Wei, J.M.; Huang, P.; Zhang, X.; Feng, B.X. Preparation of carbon quantum dots/TiO_2 nanotubes composites and their visible light catalytic applications. *J. Mater. Chem. A* **2014**, *2*, 18082–18086. [CrossRef]
12. Zhou, C.; Lai, C.; Zhang, C.; Zeng, G.; Huang, D.; Cheng, M.; Hu, L.; Xiong, W.; Chen, M.; Wang, J. Semiconductor/boron nitride composites: Synthesis, properties, and photocatalysis applications. *Appl. Catal. B Environ.* **2018**, *238*, 6–18. [CrossRef]
13. Zhu, M.; Osakada, Y.; Kim, S.; Fujitsuka, M.; Majima, T. Black phosphorus: A promising two dimensional visible and near-infrared-activated photocatalyst for hydrogen evolution. *Appl. Catal. B Environ.* **2017**, *217*, 285–292. [CrossRef]
14. Bai, X.; Sun, C.; Liu, D.; Luo, X.; Li, D.; Wang, J.; Wang, N.; Chang, X.; Zong, R.; Zhu, Y. Photocatalytic degradation of deoxynivalenol using graphene/ZnO hybrids in aqueous suspension. *Appl. Catal. B Environ.* **2017**, *204*, 11–20. [CrossRef]
15. Zhu, Y.; Wang, Y.; Ling, Q.; Zhu, Y. Enhancement of full-spectrum photocatalytic activity over $BiPO_4/Bi_2WO_6$ composites. *Appl. Catal. B Environ.* **2017**, *200*, 222–229. [CrossRef]

16. Carrasco-Jaim, O.A.; Ceballos-Sanchez, O.; Torres-Martínez, L.M.; Moctezuma, E.; Gómez-Solís, C. Synthesis and characterization of PbS/ZnO thin film for photocatalytic hydrogen production. *J. Photochem. Photobiol. A Chem.* **2017**, *347*, 98–104. [CrossRef]
17. Bi, L.; Gao, X.; Zhang, L.; Wang, D.; Zou, X.; Xie, T. Enhanced photocatalytic hydrogen evolution of NiCoP/g-C_3N_4 with the improved separation efficiency and charge transfer efficiency. *ChemSusChem* **2018**, *11*, 276–284. [CrossRef]
18. Cao, S.W.; Low, J.X.; Yu, J.G.; Jaroniec, M. Polymeric photocatalysts based on graphitic carbon nitride. *Adv. Mater.* **2015**, *27*, 2150–2176. [CrossRef]
19. Wang, K.; Li, Q.; Liu, B.S.; Cheng, B.; Ho, W.K.; Yu, J.G. Sulfur-doped g-C_3N_4 with enhanced photocatalytic CO_2-reduction performance. *Appl. Catal. B Environ.* **2015**, *176*, 44–52. [CrossRef]
20. Liu, J.; Liu, Y.; Liu, N.Y.; Han, Y.Z.; Zhang, X.; Huang, H.; Lifshitz, Y.; Lee, S.T.; Zhong, J.; Kang, Z.H. Metal-free efficient photocatalyst for stable visible water splitting via a two-electron pathway. *Science* **2015**, *347*, 970–974. [CrossRef]
21. Cao, S.W.; Yuan, Y.P.; Barber, J.; Loo, S.C.J.; Xue, C. Noble-metal-free g-C_3N_4/Ni(dmgH)2 composite for efficient photocatalytic hydrogen evolution under visible light irradiation. *Appl. Surf. Sci.* **2014**, *319*, 344–349. [CrossRef]
22. Alhaji, M.H.; Sanaullah, K.; Khan, A.; Hamza, A.; Muhammad, A.; Mustapha, S.I.; Rigit, A.R.H.; Bhawani, S.A. Recent developments in immobilizing titanium dioxide on supports for degradation of organic pollutants in wastewater—A review. *Int. J. Environ. Sci. Technol.* **2017**, *14*, 2053. [CrossRef]
23. Ma, X.; Ma, W.; Jiang, D.; Li, D.; Meng, S.; Chen, M. Construction of novel WO_3/$SnNb_2O_6$ hybrid nanosheet heterojunctions as efficient Z-scheme photocatalysts for pollutant degradation. *J. Colloid Interface Sci.* **2017**, *506*, 93–101. [CrossRef] [PubMed]
24. Zhou, C.; Lai, C.; Xu, P.; Zeng, G.; Huang, D.; Zhang, C.; Cheng, M.; Hu, L.; Wan, J.; Liu, Y. In situ grown AgI/$Bi1_2O_{17}Cl_2$ heterojunction photocatalysts for visible light degradation of sulfamethazine: Efficiency, pathway, and mechanism. *ACS Sustain. Chem. Eng.* **2018**, *6*, 4174–4184. [CrossRef]
25. Yan, S.C.; Li, Z.S.; Zou, Z.G. Photodegradation of rhodamine B and methyl orange over boron-doped g-C_3N_4 under visible light irradiation. *Langmuir* **2010**, *26*, 3894–3901. [CrossRef]
26. Huang, Z.A.; Sun, Q.; Lv, K.L.; Zhang, Z.H.; Li, M.; Li, B. Effect of contact interface between TiO_2 and g-C_3N_4 on the photoreactivity of g-C_3N_4/TiO_2 photocatalyst: (0 0 1) vs. (1 0 1) facets of TiO_2. *Appl. Catal. B Environ.* **2015**, *164*, 420–427. [CrossRef]
27. Zhang, Y.; Li, L.; Han, Q.T.; Tang, L.Q.; Chen, X.Y.; Hu, J.Q.; Li, Z.S.; Zhou, Y.; Liu, J.M.; Zou, Z.J. Bi_2MoO_6 nanostrip networks for enhanced visible-light photocatalytic reduction of CO_2 to CH_4. *ChemPhysChem* **2017**, *18*, 3240–3244. [CrossRef]
28. Sun, Z.; Fischer, J.M.T.A.; Li, Q.; Hu, J.; Tang, Q.; Wang, H.; Wu, Z.; Hankel, M.; Searles, D.J.; Wang, L. Enhanced CO_2 photocatalytic reduction on alkali-decorated graphitic carbon nitride. *Appl. Catal. B Environ.* **2017**, *216*, 146–155. [CrossRef]
29. Wang, X.C.; Maeda, K.; Thomas, A.; Takanabe, K.; Xin, G.; Carlesson, J.M.; Domen, K.; Antonietti, M. A metal-free polymeric photocatalyst for hydrogen production from water under visible light. *Nat. Mater.* **2009**, *8*, 76–80. [CrossRef]
30. Qin, L.; Zeng, G.; Lai, C.; Huang, D.; Xu, P.; Zhang, C.; Cheng, M.; Liu, X.; Liu, S.; Li, B. "Gold rush" in modern science: Fabrication strategies and typical advanced applications of gold nanoparticles in sensing. *Coord. Chem. Rev.* **2018**, *359*, 1–31. [CrossRef]
31. Wang, X.C.; Blechert, S.; Antonietti, M. Polymeric graphitic carbon nitride for heterogeneous photocatalysis. *ACS Catal.* **2012**, *2*, 1596–1606. [CrossRef]
32. Wang, Y.; Wang, X.; Antonietti, M. Polymeric graphitic carbon nitride as a heterogeneous organocatalyst: From photochemistry to multipurpose catalysis to sustainable chemistry. *Angew. Chem.* **2012**, *51*, 68–89. [CrossRef] [PubMed]
33. Jiang, Z.; Wan, W.; Li, H.; Yuan, S.; Zhao, H.; Wong, P.K. A hierarchical Z-scheme alpha-Fe_2O_3/g-C_3N_4 hybrid for enhanced photocatalytic CO_2 reduction. *Adv. Mater.* **2018**, *30*. [CrossRef]
34. Lau, V.W.; Moudrakovski, I.; Botari, T.; Weinberger, S.; Mesch, M.B.; Duppel, V.; Senker, J.; Blum, V.; Lotsch, B.V. Rational design of carbon nitride photocatalysts by identification of cyanamide defects as catalytically relevant sites. *Nat. Commun.* **2016**, *7*, 12165. [CrossRef] [PubMed]

35. Lima, M.J.; Silva, A.M.T.; Silva, C.G.; Faria, J.L. Graphitic carbon nitride modified by thermal, chemical and mechanical processes as metal-free photocatalyst for the selective synthesis of benzaldehyde from benzyl alcohol. *J. Catal.* **2017**, *353*, 44–53. [CrossRef]
36. Dong, F.; Wu, L.; Sun, Y.; Fu, M.; Wu, Z.; Lee, S.C. Efficient synthesis of polymeric g-C_3N_4 layered materials as novel efficient visible light driven photocatalysts. *J. Mater. Chem.* **2011**, *21*, 15171–15174. [CrossRef]
37. Yan, S.C.; Li, Z.S.; Zou, Z.G. Photodegradation performance of g-C_3N_4 fabricated by directly heating melamine. *Langmuir* **2009**, *25*, 10397–10401. [CrossRef] [PubMed]
38. Zhang, J.S.; Guo, F.S.; Wang, X.C. An optimized and general synthetic strategy for fabrication of polymeric carbon nitride nanoarchitectures. *Adv. Funct. Mater.* **2013**, *23*, 3008–3014. [CrossRef]
39. Zhang, Y.W.; Liu, J.H.; Wu, G.; Chen, W. Porous graphitic carbon nitride synthesized via direct polymerization of urea for efficient sunlight-driven photocatalytic hydrogen production. *Nanoscale* **2012**, *4*, 5300–5303. [CrossRef]
40. Du, A.J.; Sanvito, S.; Li, Z.; Wang, D.W.; Jiao, Y.; Liao, T.; Sun, Q.; Ng, Y.H.; Zhu, Z.H.; Amal, R. Hybrid graphene and graphitic carbon nitride nanocomposites: Gap opening, electron-hole puddle, interfacial charge transfer, and enhanced visible light response. *J. Am. Chem. Soc.* **2012**, *134*, 4393–4397. [CrossRef]
41. Tonda, S.; Kumar, S.; Kandula, S.; Shanker, V. Fe-doped and-mediated graphitic carbon nitride nanosheets for enhanced photocatalytic performance under natural sunlight. *J. Mater. Chem. A* **2014**, *2*, 6772–6780. [CrossRef]
42. Wu, J.; Yang, S.; Li, J.; Yang, Y.; Wang, G.; Bu, X.; He, P.; Sun, J.; Yang, J.H.; Deng, Y. Electron injection of phosphorus doped g-C_3N_4 quantum dots: Controllable photoluminescence emission wavelength in the whole visible light range with high quantum yield. *Adv. Opt. Mater.* **2016**, *4*, 2095–2101. [CrossRef]
43. Cermak, J.; Kral, L.; Roupcova, P. Improvement of hydrogen storage kinetics in ball-milled magnesium doped with antimony. *Int. J. Hydrogen Energy* **2017**, *42*, 6144–6151. [CrossRef]
44. Jang, E.; Kim, W.J.; Kim, D.W.; Hong, S.H.; Ali, I.; Park, Y.M.; Park, T.J. Atomic layer deposition with rotary reactor for uniform hetero-junction photocatalyst, g-C_3N_4@TiO_2 core-shell structures. *RSC Adv.* **2019**, *9*, 33180–33186. [CrossRef]
45. Feng, J.; Ma, H.Z.; Chen, T.W.; Liu, C.B.; Ma, Y.C. Passivated codoping can improve the solar-to-hydrogen efficiency of graphitic carbon nitride. *J. Phys. Chem. C* **2018**, *122*, 7296–7302. [CrossRef]
46. Jang, E.; Kim, D.W.; Hong, S.H.; Park, Y.M.; Park, T.J. Visible light-driven g-C_3N_4@ZnO heterojunction photocatalyst synthesized via atomic layer deposition with a specially designed rotary reactor. *Appl. Surf. Sci.* **2019**, *487*, 206–210. [CrossRef]
47. Zhao, W.; Yang, G.; Wang, S.; He, H.; Sun, C.; Yang, S. A novel ternary plasmonic photocatalyst: Ultrathin g-C_3N_4 nanosheet hybrided by Ag/$AgVO_3$ nanoribbons with enhanced visible-light photocatalytic performance. *Appl. Catal. B Environ.* **2015**, *165*, 335–343. [CrossRef]
48. Zheng, Y.; Yu, Z.; Ou, H.; Asiri, A.M.; Chen, Y.; Wang, X. Black phosphorus and polymeric carbon nitride heterostructure for photoinduced molecular oxygen activation. *Adv. Funct. Mater.* **2018**, *28*, 1705407. [CrossRef]
49. Gu, Q.; Liao, Y.S.; Yin, L.S.; Long, J.L.; Wang, X.X.; Xue, C. Template-free synthesis of porous graphitic carbon nitride microspheres for enhanced photocatalytic hydrogen generation with high stability. *Appl. Catal. B Environ.* **2015**, *165*, 503–510. [CrossRef]
50. Tahir, M.; Cao, C.B.; Butt, F.K.; Idrees, F.; Mahmood, N.; Ali, Z.; Aslam, I.; Tanveer, M.; Rizwan, M.; Mahmood, T. Tubular graphitic-C_3N_4: A prospective material forenergy storage and green photocatalysis. *J. Mater. Chem. A* **2013**, *1*, 13949–13955. [CrossRef]
51. Lu, X.L.; Chen, P.Z.; Jia, K.C.; Liu, S.; Wu, C.Z. Facile one step method realizing scalable production of g-C_3N_4 nanosheets and study of their photocatalytic H_2 evolution activity. *J. Mater. Chem. A* **2014**, *2*, 18924–18928. [CrossRef]
52. Niu, P.; Zhang, L.L.; Liu, G.; Cheng, H.M. Graphene-like carbon nitride nanosheets for improved photocatalytic activities. *Adv. Funct. Mater.* **2012**, *22*, 4763–4770. [CrossRef]
53. Schwinghammer, K.; Mesch, M.B.; Duppel, V.; Ziegler, C.; Senker, J.; Lotsch, B.V. Crystalline carbon nitride nanosheets for improved visible-light hydrogen evolution. *J. Am. Chem. Soc.* **2014**, *136*, 1730–1733. [CrossRef] [PubMed]

54. Chen, Y.; Huang, W.; He, D.; Yue, S.; Huang, H. Construction of heterostructured g-C_3N_4/Ag/TiO_2 microspheres with enhanced photocatalysis performance under visible-light irradiation. *ACS Appl. Mater. Interfaces* **2014**, *6*, 14405–14414. [CrossRef] [PubMed]
55. Zhang, S.; Li, J.; Wang, X.; Huang, Y.; Zeng, M.; Xu, J. In situ ion exchange synthesis of strongly coupled Ag@AgCl/g-C_3N_4 porous nanosheets as plasmonic photocatalyst for highly efficient visible-light photocatalysis. *ACS Appl. Mater. Interfaces* **2014**, *6*, 22116–22125. [CrossRef] [PubMed]
56. Wu, S.Z.; Li, K.; Zhang, W.D. On the heterostructured photocatalysts Ag_3VO_4/g-C_3N_4 with enhanced visible light photocatalytic activity. *Appl. Surf. Sci.* **2015**, *324*, 324–331. [CrossRef]
57. Liu, Y.; Yu, Y.X.; Zhang, W.D. Photoelectrochemical study on charge transfer properties of nanostructured Fe_2O_3 modified by g-C_3N_4. *Int. J. Hydrogen Energy* **2014**, *39*, 9105–9113. [CrossRef]
58. Yan, H.J.; Huang, Y. Polymer composites of carbon nitride and poly (3-hexylthiophene) to achieve enhanced hydrogen production from water under visible light. *Chem. Commun.* **2011**, *47*, 4168–4170. [CrossRef]
59. Ge, L.; Han, C.C.; Liu, J. In situ synthesis and enhanced visible light photocatalytic activities of novel PANI-g-C_3N_4 composite photocatalysts. *J. Mater. Chem.* **2012**, *22*, 11843–11850. [CrossRef]
60. He, F.; Chen, G.; Yu, Y.G.; Hao, S.; Zhou, Y.S.; Zheng, Y. Facile approach to synthesize g-PAN/g-C_3N_4 composites with enhanced photocatalytic H_2 evolution activity. *ACS Appl. Mater. Interfaces* **2014**, *6*, 7171–7179. [CrossRef]
61. Sun, Q.; Wang, P.; Yu, H.; Wang, X. In situ hydrothermal synthesis and enhanced photocatalytic H_2-evolution performance of suspended rGO/g-C_3N_4 photocatalysts. *J. Mol. Catal. A Chem.* **2016**, *424*, 369. [CrossRef]
62. Tong, Z.; Yang, D.; Shi, J.; Nan, Y.; Sun, Y.; Jiang, Z. Three-dimensional porous aerogel constructed by g-C_3N_4 and graphene oxide nanosheets with excellent visible-light photocatalytic performance. *ACS Appl. Mater. Interfaces* **2015**, *7*, 25693–25701. [CrossRef] [PubMed]
63. Wan, W.C.; Yu, S.; Dong, F.; Zhang, Q.; Zhou, Y. Efficient C_3N_4/graphene oxide macroscopic aerogel visible-light photocatalyst. *J. Mater. Chem. A* **2016**, *4*, 7823–7829. [CrossRef]
64. Liu, J.; Xu, H.; Xu, Y.; Song, Y.; Lian, J.; Zhao, Y.; Wang, L.; Huang, L.; Ji, H.; Li, H. Graphene quantum dots modified mesoporous graphite carbon nitride with significant enhancement of photocatalytic activity. *Appl. Catal. B Environ.* **2017**, *207*, 429–437. [CrossRef]
65. Lim, S.J.; Zahid, M.U.; Le, P.; Ma, L.; Entenberg, D.; Harney, A.S.; Condeelis, J.; Smith, A.M. Brightness-equalized quantum dots. *Nat. Commun.* **2015**, *6*, 8210. [CrossRef] [PubMed]
66. Lewis, N.S. Research opportunities to advance solar energy utilization. *Science* **2016**, *351*, 353–363. [CrossRef]
67. Medintz, I.L.; Stewart, M.H.; Trammell, S.A.; Susumu, K.; Delehanty, J.B.; Mei, B.C.; Melinger, J.S.; Blanco-Canosa, J.B.; Dawson, P.E.; Mattoussi, H. Quantum-dot/dopamine bioconjugates function as redox coupled assemblies for in vitro and intracellular pH sensing. *Nat. Mater.* **2010**, *9*, 676–684. [CrossRef]
68. Sun, Y.P.; Zhou, B.; Lin, Y.; Wang, W.; Fernando, K.A.S.; Pathak, P.; Meziani, M.J.; Harruff, B.A.; Wang, X.; Wang, H. Quantum-sized carbon dots for bright and colorful photoluminescence. *J. Am. Chem. Soc.* **2006**, *128*, 7756–7757. [CrossRef]
69. Krysmann, M.J.; Kelarakis, A.; Dallas, P.; Giannelis, E.P. Formation mechanism of carbogenic nanoparticles with dual photoluminescence emission. *J. Am. Chem. Soc.* **2011**, *134*, 747–750. [CrossRef]
70. Georgakilas, V.; Perman, J.; Tucek, J.; Zboril, R. Broad family of carbon nanoallotropes: Classification, chemistry, and applications of fullerenes, carbon dots, nanotubes, graphene, nanodiamonds, and combined superstructures. *Chem. Rev.* **2015**, *11*, 4744–4822. [CrossRef]
71. Yang, Z.; Ren, J.; Zhang, Z.T.; Chen, X.L.; Guan, G.Z.; Qin, L.B.; Zhang, Y.; Peng, H.S. Recent advancement of nanostructured carbon for energy applications. *Chem. Rev.* **2015**, *115*, 5159–5223. [CrossRef] [PubMed]
72. Yu, X.J.; Liu, J.J.; Yu, Y.C.; Zuo, S.L.; Li, B.S. Preparation and visible light photocatalytic activity of carbon quantum dots/TiO_2 nanosheet composites. *Carbon* **2014**, *68*, 718–724. [CrossRef]
73. Zhu, S.J.; Meng, Q.N.; Wang, L.; Zhang, J.H.; Song, Y.B.; Jin, H.; Zhang, K.; Sun, H.C.; Wang, H.Y.; Yang, B. Highly photoluminescent carbon dots for multicolor patterning, sensors, and bioimaging. *Angew. Chem. Int. Ed.* **2013**, *52*, 3953–3957. [CrossRef] [PubMed]
74. Barman, M.K.; Mitra, P.; Bera, R.; Das, S.; Pramanik, A.; Parta, A. An efficient charge separation and photocurrent generation in the carbon dot-zinc oxide nanoparticle composite. *Nanoscale* **2017**, *9*, 6791–6799. [CrossRef] [PubMed]

75. Ong, W.J.; Putri, L.K.; Tan, Y.C.; Tan, L.L.; Li, N.; Ng, Y.H.; Wen, X.M.; Chai, S.P. Unravelling charge carrier dynamics in protonated g-C_3N_4 interfaced with carbon nanodots as co-catalysts toward enhanced photocatalytic CO_2 reduction: A combined experimental and first-principles DFT study. *Nano Res.* **2017**, *10*, 1673–1696. [CrossRef]
76. De, B.; Karak, N. Recent progress in carbon dot-metal based nanohybrids for photochemical and electrochemical applications. *J. Mater. Chem. A* **2017**, *5*, 1826–1859. [CrossRef]
77. Wang, Q.; Huang, J.; Sun, H.; Zhang, K.Q.; Lai, Y. Uniform carbon dots@TiO_2 nanotube arrays with full spectrum wavelength light activation for efficient dye degradation and overall water splitting. *Nanoscale* **2017**, *9*, 16046–16058. [CrossRef]
78. Zhang, Q.; Xu, W.; Han, C.; Wang, X.; Wang, Y.; Li, Z.; Wu, W.; Wu, M. Graphene structure boosts electron transfer of dual-metal doped carbon dots in photooxidation. *Carbon* **2018**, *126*, 128–134. [CrossRef]
79. Wang, W.; Ni, Y.; Xu, Z.Z. One-step uniformly hybrid carbon quantum dots with high-reactive TiO_2 for photocatalytic application. *J. Alloys Compd.* **2015**, *622*, 303–308. [CrossRef]
80. Yu, H.; Zhang, H.C.; Huang, H.; Liu, Y.; Li, H.T.; Ming, H.; Kang, Z.H. ZnO/carbon quantum dots nanocomposites: One-step fabrication and superior photocatalytic ability for toxic gas degradation under visible light at room temperature. *New J. Chem.* **2012**, *36*, 1031–1035. [CrossRef]
81. Xie, C.; Nie, B.; Zeng, L.; Liang, F.X.; Wang, M.Z.; Luo, L.; Feng, M.; Yu, Y.; Wu, C.Y.; Wu, Y. Core-shell heterojunction of silicon nanowire arrays and carbon quantum dots for photovoltaic devices and self-driven photodetectors. *ACS Nano* **2014**, *8*, 4015–4022. [CrossRef] [PubMed]
82. Zhang, H.C.; Huang, H.; Ming, H.; Li, H.T.; Zhang, L.L.; Liu, Y.; Kang, Z.H. Carbon quantum dots/Ag_3PO_4 complex photocatalysts with enhanced photocatalytic activity and stability under visible light. *J. Mater. Chem.* **2012**, *22*, 10501–10506. [CrossRef]
83. Liu, Y.; Yu, Y.X.; Zhang, W.D. Carbon quantum dots-doped CdS microspheres with enhanced photocatalytic performance. *J. Alloys Compd.* **2013**, *569*, 102–110. [CrossRef]
84. Di, J.; Xia, J.X.; Ge, Y.P.; Li, H.P.; Ji, H.Y.; Xu, H.; Zhang, Q.; Li, H.M.; Li, M.N. Novel visible-light-driven CQDs/Bi_2WO_6 hybrid materials with enhanced photocatalytic activity toward organic pollutants degradation and mechanism insight. *Appl. Catal. B Environ.* **2015**, *168*, 51–61. [CrossRef]
85. Han, M.; Zhu, S.; Lu, S.; Song, Y.; Feng, T.; Tao, S.; Liu, J.; Yang, B. Recent progress on the photocatalysis of carbon dots: Classification, mechanism and applications. *Nano Today* **2018**, *19*, 201–218. [CrossRef]
86. Li, H.T.; Liu, R.H.; Liu, Y.; Huang, H.; Yu, H.; Ming, A.H.; Lian, S.Y.; Lee, S.T.; Kang, Z.H. Carbon nanodots: Synthesis, properties and applications. *J. Mater. Chem.* **2012**, *22*, 17470–17475. [CrossRef]
87. Lim, C.S.; Hola, K.; Ambrosi, A.; Zboril, R.; Pumera, M. Graphene and carbon quantum dots electrochemistry. *Electrochem. Commun.* **2015**, *52*, 75–79. [CrossRef]
88. Yang, S.W.; Sun, J.; Li, X.B.; Zhou, W.; Wang, Z.Y.; He, P.; Ding, G.Q.; Xie, X.M.; Kang, Z.H.; Jiang, M.H. Large-scale fabrication of heavy doped carbon quantum dots with tunable-photoluminescence and sensitive fluorescence detection. *J. Mater. Chem. A* **2014**, *2*, 8660–8667. [CrossRef]
89. Qin, J.Y.; Zeng, H.P. Photocatalysts fabricated by depositing plasmonic Ag nanoparticles on carbon quantum dots/graphitic carbon nitride for broad spectrum photocatalytic hydrogen generation. *Appl. Catal. B Environ.* **2017**, *209*, 161–173. [CrossRef]
90. Wang, F.L.; Chen, P.; Feng, Y.P.; Xie, Z.J.; Liu, Y.; Su, Y.H.; Zhang, Q.X.; Wang, Y.F.; Yao, K.; Lv, W.Y. Facile synthesis of N-doped carbon dots/g-C_3N_4 photocatalyst with enhanced visible-light photocatalytic activity for the degradation of indomethacin. *Appl. Catal. B Environ.* **2017**, *207*, 103–113. [CrossRef]
91. Zhang, M.; Lai, C.; Li, B.S.; Huang, D.L.; Zeng, G.M.; Xu, P.; Qin, L.; Liu, S.Y.; Liu, X.G.; Yi, H. Rational design 2D/2D BiOBr/CDs/g-C_3N_4 Z-scheme heterojunction photocatalyst with carbon dots as solid-state electron mediators for enhanced visible and NIR photocatalytic activity: Kinetics, intermediates, and mechanism insight. *J. Catal.* **2019**, *369*, 469–481. [CrossRef]
92. Wang, X.F.; Cheng, J.J.; Yu, H.G.; Yu, J.G. A facile hydrothermal synthesis of carbon dots modified g-C_3N_4 for enhanced photocatalytic H_2-evolution performance. *Dalton Trans.* **2017**, *46*, 6417–6424. [CrossRef] [PubMed]
93. Fang, S.; Xia, Y.; Lv, K.; Li, Q.; Sun, J.; Li, M. Effect of carbon-dots modification on the structure and photocatalytic activity of g-C_3N_4. *Appl. Catal. B Environ.* **2016**, *185*, 225–232. [CrossRef]
94. Guo, Y.; Yao, P.; Zhu, D.; Gu, C. A novel method for the development of a carbon quantum dot/carbon nitride hybrid photocatalyst that responds to infrared light irradiation. *J. Mater. Chem. A* **2015**, *3*, 13189–13192. [CrossRef]

95. Hong, Y.; Meng, Y.; Zhang, G.; Yin, B.; Zhao, Y.; Shi, W.; Li, C. Facile fabrication of stable metal-free CQDs/g-C_3N_4 heterojunctions with efficiently enhanced visible-light photocatalytic activity. *Sep. Purif. Technol.* **2016**, *171*, 229–237. [CrossRef]
96. Zhang, H.; Zhao, L.X.; Geng, F.L.; Guo, L.H.; Wan, B.; Yang, Y. Carbon dots decorated graphitic carbon nitride as an efficient metal-free photocatalyst for phenol degradation. *Appl. Catal. B Environ.* **2016**, *180*, 656–662. [CrossRef]
97. Feng, H.; Guo, Q.; Xu, Y.; Chen, T.; Zhou, Y.Y.; Wang, Y.G.; Wang, M.Z.; Shen, D.S. Surface nonpolarization of g-C_3N_4 by decoration with sensitized quantum dots for improved CO_2 photoreduction. *ChemSusChem* **2018**, *11*, 4256–4261. [CrossRef]
98. Tang, C.Y.; Liu, C.; Han, Y.; Guo, Q.Q.; Ouyang, W.; Feng, H.J.; Wang, M.Z.; Xu, F. Nontoxic carbon quantum dots/g-C_3N_4 for efficient photocatalytic inactivation of *Staphylococcus aureus* under visible light. *Adv. Healthc. Mater.* **2019**, *8*, 1801534. [CrossRef]
99. Liu, Q.; Chen, T.; Guo, Y.; Zhang, Z.G.; Fang, X.M. Ultrathin g-C_3N_4 nanosheets coupled with carbon nanodots as 2D/0D composites for efficient photocatalytic H_2 evolution. *Appl. Catal. B Environ.* **2016**, *193*, 248–258. [CrossRef]
100. Xie, Z.J.; Feng, Y.P.; Wang, F.L.; Chen, D.N.; Zhang, Q.X.; Zeng, Y.Q.; Lv, W.Y.; Liu, G.G. Construction of carbon dots modified MoO_3/g-C_3N_4 Z-scheme photocatalyst with enhanced visible-light photocatalytic activity for the degradation of tetracycline. *Appl. Catal. B Environ.* **2018**, *229*, 96–104. [CrossRef]
101. Wang, Y.; Liu, X.Q.; Liu, J.; Han, B.; Hu, X.Q.; Yang, F.; Xu, Z.W.; Li, Y.C.; Jia, S.R.; Li, Z. Carbon quantum dot implanted graphite carbon nitride nanotubes: Excellent charge separation and enhanced photocatalytic hydrogen evolution. *Angew. Chem. Int. Ed.* **2018**, *57*, 5765–5771. [CrossRef] [PubMed]
102. Wang, K.; Wang, X.Z.; Pan, H.; Liu, Y.L.; Xu, S.G.; Cao, S.K. In situ fabrication of CDs/g-C_3N_4, hybrids with enhanced interface connection via calcination of the precursors for photocatalytic H_2 evolution. *Int. J. Hydrogen Energy* **2018**, *43*, 91–99. [CrossRef]
103. Li, K.; Su, F.Y.; Zhang, W.D. Modification of g-C_3N_4 nanosheets by carbon quantum dots for highly efficient photocatalytic generation of hydrogen. *Appl. Surf. Sci.* **2016**, *375*, 110–117. [CrossRef]
104. Wang, W.J.; Zeng, Z.T.; Zeng, G.M.; Zhang, C.; Xiao, R.; Zhou, C.Y.; Xiong, W.P.; Yang, Y.; Lei, L.; Liu, Y. Sulfur doped carbon quantum dots loaded hollow tubular g-C_3N_4 as novel photocatalyst for destruction of Escherichia coli and tetracycline degradation under visible light. *Chem. Eng. J.* **2019**, *378*, 122–132. [CrossRef]
105. Jiang, X.H.; Wang, L.C.; Yu, F.; Nie, Y.C.; Xing, Q.J.; Liu, X.; Pei, Y.; Zou, J.P.; Dai, W.L. Photodegradation of organic pollutants coupled with simultaneous photocatalytic evolution of hydrogen using quantum-dot-modified g-C_3N_4 catalysts under visible-light irradiation. *ACS Sustain. Chem. Eng.* **2018**, *6*, 12695–12705. [CrossRef]
106. Jian, X.; Liu, X.; Yang, H.M.; Li, J.G.; Song, X.L.; Dai, H.Y.; Liang, Z.H. Construction of carbon quantum dots/proton-functionalized graphitic carbon nitride nanocomposite via electrostatic self-assembly strategy and its application. *Appl. Surf. Sci.* **2016**, *370*, 514–521. [CrossRef]
107. Guo, F.; Shi, W.L.; Guan, W.S.; Huang, H.; Liu, Y. Carbon dots/g-C_3N_4/ZnO nanocomposite as efficient visible-light driven photocatalyst for tetracycline total degradation. *Sep. Purif. Technol.* **2017**, *173*, 295–303. [CrossRef]
108. Li, Y.; Feng, X.H.; Lu, Z.X.; Yin, H.; Liu, F.; Xiang, Q.J. Enhanced photocatalytic H_2-production activity of C-dots modified g-C_3N_4/TiO_2 nanosheets composites. *J. Colloid Interface Sci.* **2017**, *513*, 866–876. [CrossRef]
109. Liu, Q.; Chen, T.X.; Guo, Y.R.; Zhang, Z.G.; Fang, X.M. Grafting Fe(III) species on carbon nanodots/Fe-doped g-C_3N_4 via interfacial charge transfer effect for highly improved photocatalytic performance. *Appl. Catal. B Environ.* **2017**, *205*, 173–181. [CrossRef]
110. He, H.J.; Huang, L.H.; Zhong, Z.J.; Tan, S.Z. Constructing three-dimensional porous graphene-carbon quantum dots/g-C_3N_4, nanosheet aerogel metal-free photocatalyst with enhanced photocatalytic activity. *Appl. Surf. Sci.* **2018**, *441*, 285–294. [CrossRef]
111. Xu, T.F.; Wang, D.N.; Dong, L.L.; Shen, H.B.; Lu, W.Y.; Chen, W.X. Graphitic carbon nitride co-modified by zinc phthalocyanine and graphene quantum dots for the efficient photocatalytic degradation of refractory contaminants. *Appl. Catal. B Environ.* **2019**, *244*, 96–106. [CrossRef]
112. Yuan, A.L.; Lei, H.; Xi, F.N.; Liu, J.Y.; Qin, L.S.; Chen, Z.; Dong, X.P. Graphene quantum dots decorated graphitic carbon nitride nanorods for photocatalytic removal of antibiotics. *J. Colloid Interface Sci.* **2019**, *548*, 56–65. [CrossRef]

113. Wang, Y.P.; Li, Y.K.; Zhao, J.L.; Wang, J.S.; Li, Z.J. g-C_3N_4/B doped g-C_3N_4 quantum dots heterojunction photocatalysts for hydrogen evolution under visible light. *Int. J. Hydrogen Energy* **2019**, *44*, 618–628. [CrossRef]
114. Wang, H.; Yuan, X.Z.; Wang, H.; Chen, X.H.; Wu, Z.B.; Jiang, L.B.; Xiong, W.P.; Zeng, G.M. Facile synthesis of Sb_2S_3/ultrathin g-C_3N_4 sheets heterostructures embedded with g-C_3N_4 quantum dots with enhanced NIR-light photocatalytic performance. *Appl. Catal. B Environ.* **2016**, *193*, 36–46. [CrossRef]
115. Zhao, T.Y.; Xing, Z.P.; Xiu, Z.Y.; Li, Z.Z.; Yang, S.L.; Zhou, W. Oxygen-doped MoS_2 nanospheres/CdS quantum dots/g-C_3N_4 nanosheets super-architectures for prolonged charge lifetime and enhanced visible-light-driven photocatalytic performance. *ACS Appl. Mater. Interfaces* **2019**, *11*, 7104–7111. [CrossRef] [PubMed]
116. Chen, W.; Liu, T.Y.; Huang, T.; Liu, X.H.; Zhu, J.W.; Duan, G.R.; Yang, X.J. In situ fabrication of novel Z-scheme Bi_2WO_6 quantum dots/g-C_3N_4 ultrathin nanosheets heterostructures with improved photocatalytic activity. *Appl. Surf. Sci.* **2015**, *355*, 379–387. [CrossRef]
117. Chen, T.J.; Quan, W.; Yu, L.B.; Hong, Y.Z.; Song, C.J.; Fan, M.S.; Xiao, L.S.; Gu, W.; Shi, W.D. One-step synthesis and visible-light-driven H_2 production from water splitting of Ag quantum dots/g-C_3N_4 photocatalysts. *J. Alloy Compd.* **2016**, *686*, 628–634. [CrossRef]
118. Han, C.Q.; Li, J.; Ma, Z.Y.; Xie, H.Q.; Waterhouse, G.I.N.; Ye, L.Q.; Zhang, T.R. Black phosphorus quantum dot/g-C_3N_4 composites for enhanced CO_2 photoreduction to CO. *Sci. China Mater.* **2018**, *61*, 1159–1166. [CrossRef]
119. Ye, M.Y.; Zhao, Z.H.; Hu, Z.F.; Liu, L.Q.; Ji, H.M.; Shen, Z.R.; Ma, T.Y. 0D/2D heterojunctions of vanadate quantum dots/graphitic carbon nitride nanosheets for enhanced visible-light-driven photocatalysis. *Angew. Chem. Int. Ed.* **2017**, *56*, 8407–8411. [CrossRef]
120. Hao, Q.G.; Mo, Z.; Chen, Z.G.; She, X.J.; Xu, Y.G.; Song, Y.H.; Ji, H.Y.; Wu, X.Y.; Yuan, S.Q.; Xu, H. 0D/2D Fe_2O_3 quantum dots/g-C_3N_4 for enhanced visible-light-driven photocatalysis. *Colloid Surf. A* **2018**, *541*, 188–194. [CrossRef]
121. Zhang, H.Y.; Tian, W.J.; Zhou, L.; Sun, H.Q.; Tadea, M.; Wang, S.B. Monodisperse Co_3O_4 quantum dots on porous carbon nitride nanosheets for enhanced visible-light-driven water oxidation. *Appl. Catal. B Environ.* **2018**, *223*, 2–9. [CrossRef]
122. Gao, G.P.; Jiao, Y.; Ma, F.X.; Jiao, Y.L.; Waclawika, E.; Du, A.G. Carbon nanodot decorated graphitic carbon nitride: New insights into the enhanced photocatalytic water splitting from ab initio studies. *Phys. Chem. Chem. Phys.* **2015**, *17*, 31140–31144. [CrossRef] [PubMed]
123. Li, H.; He, X.; Liu, Y.; Huang, H.; Lian, S.; Lee, S.T. One-step ultrasonic synthesis of water-soluble carbon nanoparticles with excellent photoluminescent properties. *Carbon* **2011**, *49*, 605–609. [CrossRef]
124. Ma, Z.; Ming, H.; Huang, H.; Liu, Y.; Kang, Z. One-step ultrasonic synthesis of fluorescent N-doped carbon dots from glucose and their visible-light sensitive photocatalytic ability. *New J. Chem.* **2012**, *36*, 861–864. [CrossRef]
125. Yu, J.; Xu, C.X.; Tian, Z.S.; Lin, Y.; Shi, Z.L. Facilely synthesized N-doped carbon quantum dots with high fluorescent yield for sensing Fe^{3+}. *New J. Chem.* **2016**, *40*, 2083–2088. [CrossRef]
126. Michalet, X.; Pinaud, F.F.; Bentolila, L.A.; Tsay, J.M.; Doose, S.; Li, J.J.; Sundaresan, G.; Wu, A.M.; Gambhir, S.S.; Weiss, S. Quantum dots for live cells, in vivo imaging, and diagnostics. *Science* **2005**, *307*, 538–544. [CrossRef]
127. Li, Y.; Zhao, Y.; Cheng, H.; Hu, Y.; Shi, G.; Dai, L.; Qu, L. Nitrogen-doped graphene quantum dots with oxygen-rich functional groups. *J. Am. Chem. Soc.* **2012**, *134*, 15–18. [CrossRef]
128. Hu, C.; Liu, Y.; Yang, Y.; Cui, J.; Huang, Z.; Wang, Y.; Yang, L.; Wang, H.; Xiao, Y.; Rong, J. One-step preparation of nitrogen-doped graphene quantum dots from oxidized debris of graphene oxide. *J. Mater. Chem. B* **2013**, *1*, 39–42. [CrossRef]
129. Wang, W.P.; Lu, Y.C.; Huang, H.; Feng, J.J.; Chen, J.R.; Wang, A.J. Facile synthesis of water-soluble and biocompatible fluorescent nitrogen-doped carbon dots for cell imaging. *Analyst* **2014**, *139*, 1692–1696. [CrossRef]
130. Wang, L.; Zhang, L.L.; Bai, L.; Han, L.; Dong, S.J. Nitrogen, cobalt-codoped carbon electrocatalyst for oxygen reduction reaction using soy milk and cobalt salts as precursors. *Electrochem. Commun.* **2013**, *34*, 68–72. [CrossRef]
131. Wang, L.; Yin, Y.; Jain, A.; Zhou, H.S. Aqueous phase synthesis of highly luminescent, nitrogen-doped carbon dots and their application as bioimaging agents. *Langmuir* **2014**, *30*, 14270–14275. [CrossRef] [PubMed]

132. Yang, Z.; Xu, M.H.; Liu, Y.; He, F.J.; Gao, F.; Su, Y.J.; Wei, H.; Zhang, Y.F. Nitrogen-doped, carbon-rich, highly photoluminescent carbon dots from ammonium citrate. *Nanoscale* **2014**, *6*, 1890–1895. [CrossRef] [PubMed]
133. Niu, J.J.; Gao, H.; Wang, L.T.; Xin, S.Y.; Zhang, G.Y.; Wang, Q.; Guo, L.N.; Liu, W.J.; Gao, X.P.; Wang, Y.H. Facile synthesis and optical properties of nitrogen-doped carbon dots. *New J. Chem.* **2014**, *38*, 1522–1527. [CrossRef]
134. Adhikari, S.P.; Hood, Z.D.; Wang, H.; Peng, R.; Kralla, A.; Lia, H.; Chend, V.W.; Morec, K.L.; Wu, Z.L.; Geyera, S. Enhanced visible light photocatalytic water reduction from a g-C_3N_4/$SrTa_2O_6$ heterojunction. *Appl. Catal. B Environ.* **2017**, *217*, 448–458. [CrossRef]
135. Zhao, Z.; Sun, Y.; Dong, F. Graphitic carbon nitride based nanocomposites: A review. *Nanoscale* **2015**, *7*, 15–37. [CrossRef] [PubMed]
136. Lin, B.; Chen, S.; Dong, F.; Yang, G. A ball-in-ball g-C_3N_4@SiO_2 nano-photoreactor for highly efficient H_2 generation and NO removal. *Nanoscale* **2017**, *9*, 5273–5279. [CrossRef]
137. Qu, D.; Liu, J.; Miao, X.; Han, M.; Zhang, H.; Cui, Z.; Sun, S.; Kang, Z.; Fan, H.; Sun, Z. Peering into water splitting mechanism of g-C_3N_4-carbon dots metal-free photocatalyst. *Appl. Catal. B Environ.* **2018**, *227*, 418–424. [CrossRef]
138. Yu, X.; Li, Z.; Liu, J.; Hu, P. TaOC chemical bond enhancing charge separation between Ta^{4+} doped Ta_2O_5 quantum dots and cotton-like g-C_3N_4. *Appl. Catal. B Environ.* **2017**, *205*, 271–280. [CrossRef]
139. Wang, F.; Wang, Y.; Feng, Y.; Zeng, Y.; Xie, Z.; Zhang, Q.; Su, Y.; Chen, P.; Liu, Y.; Yao, K. Novel ternary photocatalyst of single atom-dispersed silver and carbon quantum dots co-loaded with ultrathin g-C_3N_4 for broad spectrum photocatalytic degradation of naproxen. *Appl. Catal. B Environ.* **2018**, *221*, 510–520. [CrossRef]
140. Wang, W.; Feng, W.; Du, J.; Xue, W.; Zhang, L.; Zhao, L.; Li, Y.; Zhong, X. Cosensitized quantum dot solar cells with conversion efficiency over 12%. *Adv. Mater.* **2018**, *30*, 1705746. [CrossRef]
141. Li, J.; Cushing, S.K.; Bright, J.; Meng, F.; Senty, T.R.; Zheng, P.; Bristow, A.D.; Wu, N. Ag@Cu_2O core-shell nanoparticles as visible-light plasmonic photocatalysts. *ACS Catal.* **2013**, *3*, 47–51. [CrossRef]
142. Ingram, D.B.; Christopher, P.; Bauer, J.L.; Linic, S. Predictive model for the design of plasmonic metal/semiconductor composite photocatalysts. *ACS Catal.* **2011**, *1*, 1441–1447. [CrossRef]
143. Masih, D.; Ma, Y.; Rohani, S. Graphitic C_3N_4 based noble-metal-free photocatalyst systems: A review. *Appl. Catal. B Environ.* **2017**, *206*, 556–588. [CrossRef]
144. Yang, S.; Gong, Y.; Zhang, J.; Zhan, L.; Ma, L.; Fang, Z.; Vajtai, R.; Wang, X.; Ajayan, P.M. Exfoliated graphitic carbon nitride nanosheets as efficient catalysts for hydrogen evolution under visible light. *Adv. Mater.* **2013**, *25*, 2452–2456. [CrossRef]
145. Wang, W.N.; Huang, C.X.; Zhang, C.Y.; Zhao, M.L.; Zhang, J.; Chen, H.J.; Zha, Z.B.; Zhao, T.; Qian, H.S. Controlled synthesis of upconverting nanoparticles/$Zn_xCd_{1-x}S$ yolk-shell nanoparticles for efficient photocatalysis driven by NIR light. *Appl. Catal. B Environ.* **2018**, *224*, 854–862. [CrossRef]
146. Pan, D.; Zhang, J.; Li, Z.; Wu, M. Hydrothermal route for cutting graphene sheets into blue-luminescent graphene quantum dots. *Adv. Mater.* **2010**, *22*, 734–738. [CrossRef]
147. Li, L.L.; Ji, J.; Fei, R.; Wang, C.Z.; Lu, Q.; Zhang, J.R. A facile microwave avenue to electrochemiluminescent two-color graphene quantum dots. *Adv. Funct. Mater.* **2012**, *22*, 2971–2979. [CrossRef]
148. Qu, D.; Zheng, M.; Du, P.; Zhou, Y.; Zhang, L.G.; Li, D. Highly luminescent S, N co-doped graphene quantum dots with broad visible absorption bands for visible light photocatalysts. *Nanoscale* **2013**, *5*, 12272–12277. [CrossRef] [PubMed]
149. He, L.M.; Jing, L.Q.; Luan, Y.B.; Wang, L.; Fu, H.G. Enhanced visible activities of α-Fe_2O_3 by coupling N-doped graphene and mechanism insight. *ACS Catal.* **2014**, *4*, 990–998. [CrossRef]
150. Xu, C.Y.; Han, Q.; Zhao, Y.; Wang, L.X.; Li, Y.; Qu, L.T. Sulfur-doped graphitic carbon nitride decorated with graphene quantum dots for an efficient metal-free electrocatalyst. *J. Mater. Chem. A* **2015**, *3*, 1841–1846. [CrossRef]
151. Deng, Y.C.; Tang, L.; Feng, C.Y.; Zeng, G.M.; Wang, J.J.; Lu, Y.; Liu, Y.N.; Yu, J.F.; Chen, S.; Zhou, Y.Y. Construction of plasmonic Ag and nitrogen-doped graphene quantum dots co-decorated ultrathin graphitic carbon nitride nanosheet composites with enhanced photocatalytic activity: Full-spectrum response ability and mechanism insight. *ACS Appl. Mater. Interfaces* **2017**, *9*, 42816–42828. [CrossRef]

152. Feng, C.Y.; Deng, Y.C.; Tang, L.; Zeng, G.M.; Wang, J.J.; Yu, J.F.; Liu, Y.N.; Peng, B.; Feng, H.P.; Wang, J.J. Core-shell Ag_2CrO_4/N-GQDs@g-C_3N_4 composites with anti-photocorrosion performance for enhanced full-spectrum-light photocatalytic activities. *Appl. Catal. B Environ.* **2018**, *239*, 525–536. [CrossRef]
153. Wu, Y.; Tao, L.; Zhao, J.; Yue, X.; Deng, W.; Li, Y.; Wang, C. TiO_2/g-C_3N_4 nanosheets hybrid photocatalyst with enhanced photocatalytic activity under visible light irradiation. *Res. Chem. Intermed.* **2016**, *42*, 3609–3624. [CrossRef]
154. Wang, J.; Chen, Y.; Shen, Y.; Liu, S.; Zhang, Y. Coupling polymorphic nanostructured carbon nitrides into an isotype heterojunction with boosted photocatalytic H_2 evolution. *Chem. Commun.* **2017**, *53*, 2978–2981. [CrossRef] [PubMed]
155. Zhou, L.; Tian, Y.H.; Lei, J.Y.; Wang, L.Z.; Liu, Y.D.; Zhang, J.L. Self-modification of g-C_3N_4 with its quantum dots for enhanced photocatalytic activity. *Catal. Sci. Technol.* **2018**, *8*, 2617–2623. [CrossRef]
156. Xiao, F.; Miao, J.; Liu, B. Layer-by-layer self-assembly of CdS quantum dots/graphene nanosheets hybrid films for photoelectrochemical and photocatalytic applications. *Am. Chem. Soc.* **2014**, *136*, 1559–1569. [CrossRef] [PubMed]
157. Lin, H.; Li, Y.; Li, H.; Wang, X. Multi-node CdS hetero-nanowires grown with defect-rich oxygen-doped MoS_2 ultrathin nanosheets for efficient visible-light photocatalytic H_2 evolution. *Nano Res.* **2017**, *10*, 1377–1392. [CrossRef]
158. Wang, H.; Xu, S.; Tsai, C.; Li, Y.; Liu, C.; Zhao, J.; Liu, Y.; Yuan, H.; Abild-Pedersen, F.; Prinz, F.B. Direct and continuous strain control of catalysts with tunable battery electrode materials. *Science* **2016**, *354*, 1031–1036. [CrossRef]
159. Viswanatha, R.; Battaglia, D.M.; Curtis, M.E.; Mishima, T.D.; Johnson, M.B.; Peng, X. Shape control of doped semiconductor nanocrystals (d-dots). *Nano Res.* **2008**, *1*, 138–144. [CrossRef]
160. Zheng, D.D.; Zhang, G.G.; Wang, X.C. Integrating CdS quantum dots on hollow graphitic carbon nitride nanospheres for hydrogen evolution photocatalysis. *Appl. Catal. B Environ.* **2015**, *179*, 479–488. [CrossRef]